Dalton Transactions

ROYAL SOCIETY OF CHEMISTRY

PAPER

View Article Online
View Journal

Cite this: DOI: 10.1039/d6dt00813e

Investigation of metal identity on the structure and electronic properties of dinuclear Mn and Co complexes with triaryl tetradentate ligands

Darby H. Duffy,†[a] Dunya Sembukuttiarachchige,†[a] Athrry K. Yaddehige,[a] Soumen Sinhababu,[c] Megan M. Wilson,[a] Alexander Goodrich,[a] Daniel K. Unruh,[b] Matthew P. Shores,[c] Scott K. Shaw,[a] Bess Vlaisavljevich *[a] and Scott R. Daly *[a]

We report dinuclear Mn(II) and Co(II) complexes supported by triaryl tetradentate ligands derived from *o*-phenylenediamide that are flanked by different metal-donor substituents (X = NMe_2 *vs.* SMe). Single-crystal XRD data revealed that the Mn complexes (**Mn-1** and **Mn-2**) both possess Mn_2N_2 diamond cores with relatively similar bond distances, electronic structures, and magnetic properties regardless of the ligand identity. The Co complexes, by contrast, revealed dramatic substituent-dependent differences. Like Mn, the Co complexes were dinuclear, but their core structures varied from open (X = NMe_2; no μ-N bridging; **Co-1a**) to closed (X = SMe; intact Co_2N_2 diamond core; **Co-2**), with a second structure isolated with X = NMe_2 in between (semi-open core; **Co-1b**). Of the three structures, **Co-2** had the shortest metal–metal distance of 2.4540(8) Å, just at the onset of that expected for Co–Co bonding. Evidence of an appreciable metal–metal interaction in **Co-2** was revealed with a unique UV-vis absorption at 516 nm that was assigned to metal–metal charge transfer (MMCT). Moreover, magnetic measurements conducted on **Co-2** revealed a magnetic moment of 1.2μ_B at room temperature, which was much lower than that of other Co and Mn complexes. Active space calculations corroborated the experimental observations and suggested that **Co-2** possesses a weak metal–metal bond with a low effective bond order of 0.24. These findings, which are compared to those previously reported for Fe(II) and Cr(II) complexes with the same ligands, reveal the marked influence that metal identity has on the structures, magnetic properties, and metal–metal bonding within this family of triaryl tetradentate ligands.

Received 8th April 2026,
Accepted 8th May 2026

DOI: 10.1039/d6dt00813e

rsc.li/dalton

Introduction

Dinuclear (or binuclear) first-row transition metal complexes exhibit rich electronic properties and reactivities that are exquisitely sensitive to the surrounding ligand framework, metal identity, and local coordination environment.[1] Unlike dinuclear complexes with 4d and 5d transition metals that tend to be low-spin, the prevalence of high-spin configurations with 3d metals (especially in the presence of weak-field ligands) can yield variable coupling of unpaired electrons and magnetic exchange that is often facilitated by bridging ligands in the dinuclear core (*i.e.* superexchange).[2] The metals may also exhibit through-space interactions, with the strongest of these giving rise to formal metal–metal bonds.[1–3] The unique electronic and bonding configurations afforded in these complexes can promote reactions that are otherwise inaccessible using a single metal center.[4–6] In this context, nature exploits bimetallic active sites to perform important reactions in metalloproteins,[7–11] which continues to inspire the intentional design of dinucleating ligands and complexes capable of leveraging two first-row metals for small molecule transformations and catalysis.[12–24]

Chelating ligands containing *o*-phenylenediamide and related subunits are effective in forming multinuclear first-row transition metal complexes. The arene confers rigidity in ligand scaffolds, and amido ligands are known to readily bridge 3d metals and form M–N–M linkages. Betley and co-workers, for example, have conducted extensive work with tripodal ligands decorated with *o*-phenylenediamide-derived

[a]*Department of Chemistry, The University of Iowa, Iowa City, IA 52442, USA. E-mail: scott-daly@uiowa.edu, bess-vlaisavljevich@uiowa.edu*
[b]*The University of Iowa, Office of the Vice President for Research, 2660 UCC, Iowa City, Iowa 52242, USA*
[c]*Department of Chemistry, Colorado State University, Fort Collins, Colorado 80523, USA*
†Co-first authors. These authors may swap the order of their names on their CVs.

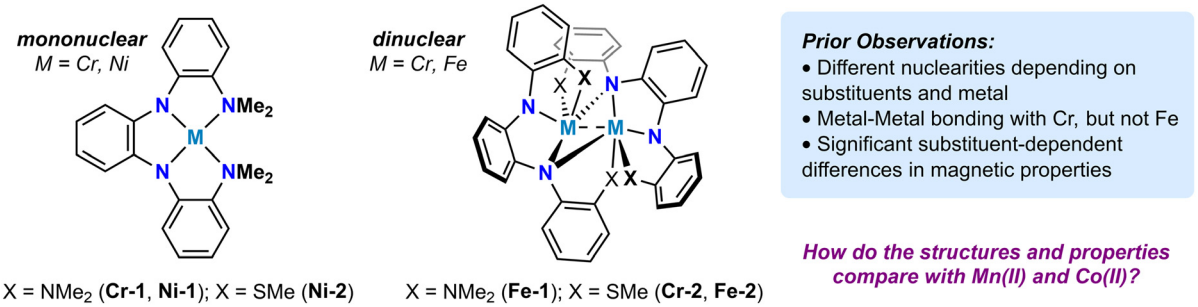

Fig. 1 Summary of the results reported previously with ligands **L1** (X = NMe_2) and **L2** (X = SMe) with divalent Cr, Fe, and Ni.[62–64]

arms and shown how they can form Mn, Fe, and Co clusters containing up to six metals.[25–43] Rigid NNN pincer and related ligands derived from bis(2-aminophenyl)amine have been used by several groups to prepare dinuclear complexes with Co, Ni, and Cu.[44–48] More recently, Hernández Sánchez and co-workers demonstrated how dinuclear complexes with most of the first-row metals can be prepared by appending similar 2-aminophenyl groups to 1,4,7,10-tetraazacyclododecane (cyclen).[49] Related dinucleating ligands have been employed with first-row metals, including macrocycles comprised of two pyridine dialdimine (PDI) subunits reported by Tomson,[50–60] and a flexible tetraamidodiamide scaffold described by Desnoyer.[61]

In 2024, we reported that triaryl tetradentate ligands derived from *o*-phenylenediamide are capable of forming diiron complexes, with significant differences in structure and electronic properties depending on the identity of the flanking donor group (Fig. 1).[63] For example, the Fe–Fe distance with **L1** (X = NMe_2) in [Fe_2(**L1**)$_2$] (**Fe-1**) was 2.5072(5) Å whereas this distance in [Fe_2(**L2**)$_2$] (X = SMe; **Fe-2**) was 2.7666(6) Å. More recently, we showed that the structural differences are even more dramatic with Cr(II) analogs, so much so that the change in donor groups induced a change in nuclearity.[64] The X = NMe_2 donor groups in **L1** yielded the mononuclear square planar complex Cr(**L1**) (**Cr-1**), similar to those described by some of us with Ni(II),[62] whereas the dinuclear complex [Cr_2(**L2**)$_2$] (**Cr-2**) was formed with X = SMe. The Cr–Cr distance in **Cr-2** was remarkably short at 2.3356(6) Å, and active-space calculations indicated that the short distance could be ascribed to Cr–Cr bonding. Temperature-dependent magnetism studies conducted on the dinuclear Fe and Cr complexes revealed significant differences in antiferromagnetic coupling due to metal- and substituent-driven changes in the dinuclear structure.[64,65]

The differing structures and associated electronic properties observed previously with Cr and Fe naturally led to questions as to how they might vary with other 3d metals, especially with Mn and Co. Continuing to build on our prior work, herein we report the syntheses, structures, and magnetic properties of Mn(II) and Co(II) complexes with **L1** and **L2**. The results show that dinuclear complexes are formed with both metals, albeit with metal- and ligand-dependent structure variations that differ significantly compared to those with Fe(II) and Cr(II).

Results and discussion

Synthesis of dinuclear complexes

In our preliminary communication,[63] we found that treating Fe[$N(SiMe_3)_2$]$_2$ with H_2(**L1**) and H_2(**L2**) in benzene afforded clean aminolysis reactions to yield **Fe-1** and **Fe-2**, which could be isolated as single crystals in yields of 67% and 85%, respectively. We found that similar reactions can be used to prepare dinuclear complexes with Mn(II) and Co(II) (Scheme 1). The reaction of Co[$N(SiMe_3)_2$]$_2$(THF)[66,67] with H_2(**L1**) and H_2(**L2**) in THF yielded **Co-1** and **Co-2**, respectively. Both complexes were confirmed to be dinuclear based on single-crystal X-ray diffraction (XRD) studies (see below). Similarly, the reaction of H_2(**L2**) with *in situ* prepared Mn_2[$N(SiMe_3)_2$]$_4$ [68,69] afforded **Mn-2**, which was isolated as green crystals in 67% yield from concentrated benzene and pentane solutions. Attempts to prepare **Mn-1** using the same route with H_2(**L1**) and Mn_2[$N(SiMe_3)_2$]$_4$ were unsuccessful in our hands; only incomplete reaction products like Mn[H(**L1**)]$_2$ were crystallized from the reaction mixtures (Fig. S1; SI). However, swapping out the Mn_2[$N(SiMe_3)_2$]$_4$ starting material for $Mn_2(Mes)_4(THF)_2$ [70] (Mes = mesityl) afforded green **Mn-1**, which could be isolated as single crystals in a moderate yield (48%).

Structural comparisons

Single-crystal XRD analysis of **Mn-1** and **Mn-2** revealed that both complexes are dinuclear in the solid state (Fig. 2), as observed previously with **Fe-1** and **Fe-2**. In contrast to the Fe complexes, which showed a 0.26 Å difference in Fe–Fe distances depending on the identity of the flanking ligand substituents (NMe_2 *vs.* SMe),[63] the Mn–Mn distances in **Mn-1** and **Mn-2** are similar at 2.7584(5) and 2.7984(8) Å, respectively (Table 1). The coordination geometry around each metal in both complexes is best described as distorted square pyramidal (τ_5 = 0.05–0.29;[71,72] Table 1). The bridging metal–amido distances ($N_{bridging}$) in the Mn_2N_2 core are asymmetric like those in the Fe complexes (more so in **Mn-1**) with each bridging ligand forming an X-type Mn–$N_{bridging}$ bond to one metal

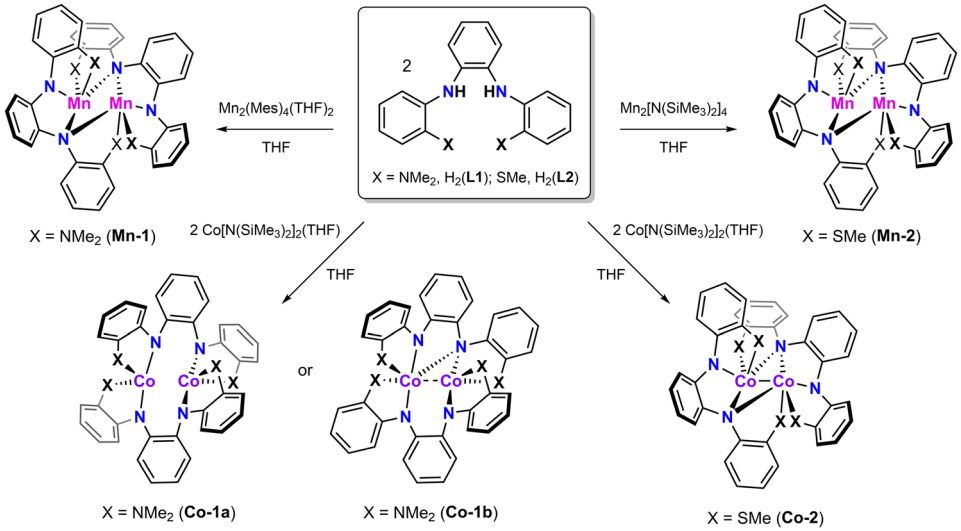

Scheme 1 Synthesis of dinuclear Mn(II) and Co(II) complexes with H_2(**L1**) and H_2(**L2**).

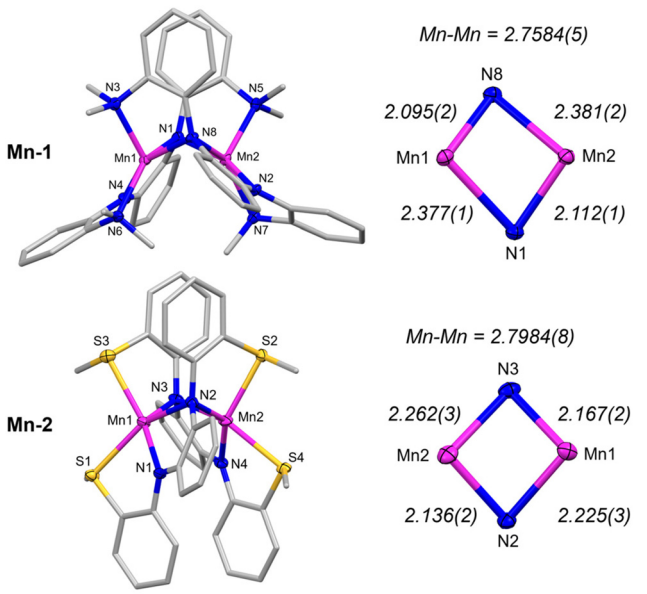

Fig. 2 Left – molecular structures of **Mn-1** and **Mn-2**. Ellipsoids are drawn at 50% probability. Hydrogen atoms and co-crystallized solvent molecules were omitted, and carbon atoms are shown as capped sticks. Right – comparison of atomic distances (Å) in the Mn_2N_2 cores.

and an L-type Mn ← $N_{bridging}$ bond to the other, as shown in Fig. 2. The terminal metal–amido ($N_{terminal}$) distances are shorter in **Mn-1** at 2.031(2) and 2.038(1) Å and increase slightly to 2.083(6) and 2.102(6) Å in **Mn-2**. The Mn–S distances in **Mn-2** range from 2.564(1) to 2.644(1) Å, which are comparable to those reported for other Mn(II) complexes containing chelating thioether ligands.[73–79]

The structures of **Mn-1** and **Mn-2** reveal that the Mn_2N_2 cores are significantly puckered, as observed for dinuclear Fe and Cr complexes with the same ligands. The relatively rigid and chelating nature of **L1** and **L2** causes the M_2N_2 cores to fold to accommodate both the bridging amido ligands and coordination of the remaining ligand donors at sites around the metal. The extent of folding can be quantified using the hinge angle,[64] which we have defined as the M–N_{cent}–M angle, where N_{cent} is the calculated centroid between the two bridging N atoms. The Mn–N_{cent}–Mn angle is 123.4° for **Mn-1** and 119.1° for **Mn-2**, which is larger than that reported previously for **Cr-2** at 111.7°.[64] We showed previously that the more acute hinge angle in **Cr-2** correlates with the presence of significant Cr–Cr bonding; the decreased angle brings the metals closer together and facilitates increased overlap of the 3d-orbitals. Betley and coworkers have described similar phenomena in triiron clusters supported by bridging *o*-phenylenediamido units.[80]

Single-crystal XRD studies of **Co-1** and **Co-2** also revealed them to be dinuclear complexes in the solid state, albeit with more dramatic substituent-driven differences in the dinuclear core compared to the Mn complexes (Fig. 3 and 4). The structure of **Co-2** with X = SMe possesses a dinuclear core with a relatively short Co–Co distance of 2.4539(4) Å and nearly symmetric bridging Co–$N_{bridging}$ distances of 1.961(2)–1.983(2) Å (Fig. 3). For comparison, most Co(II) complexes containing dinuclear Co_2N_2 cores bridged by secondary amido ligands have Co–Co distances that range from 2.55 to 2.68 Å,[44,69,81–84] although examples with shorter distances similar to **Co-2** have been reported recently by the groups of Hevia and Power.[85–87] The Co_2N_2 diamond core of **Co-2** shows a puckered hinge angle of 118.7°, similar to that of **Mn-2**. The Co–S distances range from 2.2214(6) to 2.3165(7) Å. These distances are significantly shorter than those observed for **Mn-2**, but they are consistent with the differences reported for other isomorphous Co(II) and Mn(II) complexes containing metal–thioether bonds.[75]

In contrast to **Co-2**, two structures were identified in crystalline samples of **Co-1** (X = NMe_2), neither possessing a fully

Table 1 Comparison of distances (Å), angles (°), and geometry indices (τ) from XRD structures of **M-1** and **M-2** complexes with M = Mn, Fe, and Co. Bridging and non-bridging amido ligands are distinguished as N_b and N_t, respectively

Complex X =	**Mn-1** NMe_2	**Mn-2** SMe	**Fe-1** [63] NMe_2	**Fe-1a** [63] NMe_2	**Fe-2** [63] SMe	**Co-1a** NMe_2	**Co-1b** NMe_2	**Co-2** SMe
M–M	2.7584(5)	2.7984(8)	2.5072(5)	2.627(2)	2.7666(6)	2.880(1)	2.6364(6)	2.4540(8)
M–N_b	2.095(2)	2.136(2)	2.082(1)		2.051(2)		2.428(2)	1.961(2)
	2.112(1)	2.167(2)	2.097(1)		2.056(2)		1.9741(2)	1.977(2)
	2.377(1)	2.225(3)	2.290(1)		2.236(2)			1.983(2)
	2.381(2)	2.262(3)	2.305(1)		2.286(2)			1.972(2)
M–N_t	2.031(2)	2.083(6)	1.969(1)	1.964(5)	1.989(2)	1.951(2)	1.924(2)	1.906(2)
	2.038(1)	2.102(2)	1.980(1)	1.969(6)	1.997(2)		1.976(2)	1.915(2)
				2.012(6)			1.943(2)	
				2.030(5)				
M–X	2.192(1)	2.564(1)	2.179(1)	2.148(6)	2.4243(7)	2.149(3)	2.222(2)	2.316(1)
	2.196(2)	2.566(1)	2.180(1)	2.165(8)	2.4265(7)		2.097(2)	2.2214(7)
	2.389(2)	2.606(8)	2.383(1)	2.241(8)	2.5631(7)		2.095(2)	2.3150(9)
	2.403(1)	2.644(1)	2.409(1)	2.289(6)	2.5769(8)		2.264(2)	2.226(1)
M–N_b–M	75.56(5)	78.33(8)	69.25(4)		78.97(6)		72.76(7)	77.08(8)
	75.58(5)	79.90(8)	69.80(4)		80.26(7)			76.71(6)
N_b–M–N_b	91.28(5)	88.87(9)	95.90(5)		94.83(7)			87.38(8)
	91.81(5)	89.05(9)	95.96(5)		96.19(7)			87.52(7)
M–N_{cent}–M	123.4	119.1	116.9		144.5			118.7
$\tau_5(\tau_4;\tau_4')$	0.29/0.07	0.20/0.05	0.34/0.14	(0.62;0.46)	0.06/0.00	(0.69; 0.60)	0.20 (0.65; 0.50)	0.01/0.00

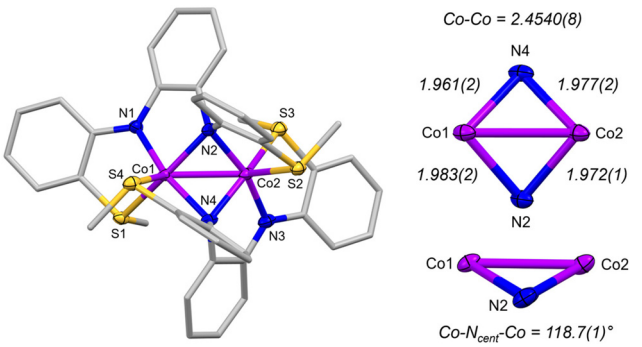

Fig. 3 Molecular structure of **Co-2**. Ellipsoids are drawn at 50% probability. Hydrogen atoms and co-crystallized solvent molecules were omitted, and carbon atoms are shown as capped sticks.

intact Co_2N_2 core. The first product, distinguished here as **Co-1a**, contains an "open" dinuclear core with no bridging Co–amido bonds (Fig. 4). The structure has approximate D_2 point group symmetry, and the coordination environment around each Co is four-coordinate and best described as distorted tetrahedral ($\tau_4 = 0.69; \tau_4' = 0.60$).[88,89] The Co–Co distance in **Co-1a** is 2.8805(9) Å, which is approximately 0.43 Å longer than that observed in **Co-2**. The second species, designated as **Co-1b**, has a half-open dinuclear core. This structure has a single bridging amido ligand with asymmetric Co–$N_{bridging}$ distances of 1.974(2) and 2.438(2) Å. Reflecting its intermediate nature between **Co-2** and **Co-1a**, the Co–Co distance in **Co-1b** is 2.6365(6) Å. The isolation of both **Co-1a** and **Co-1b** likely arises due to differences in crystal packing, suggesting small energy

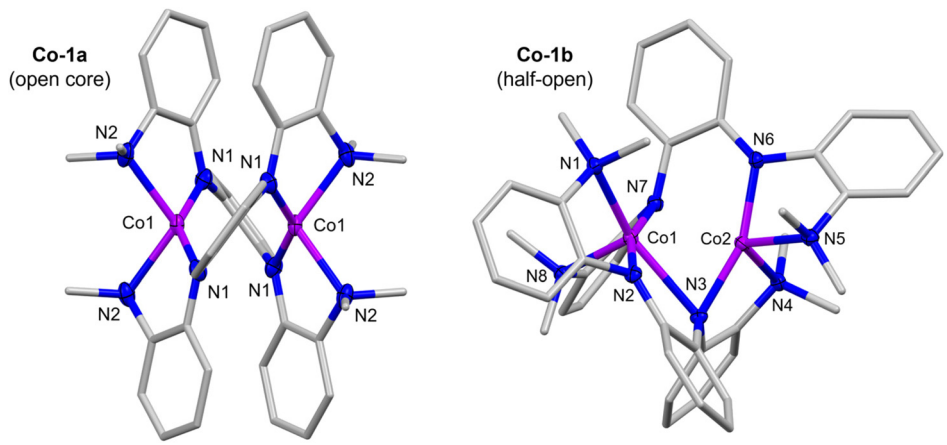

Fig. 4 Comparison of the molecular structures of **Co-1a** and **Co-1b**. Ellipsoids are drawn at 50% probability. Hydrogen atoms and co-crystallized solvent molecules were omitted, and carbon atoms are shown as capped sticks.

differences between the two structures. Similar observations were made previously in studies of **Fe-1**. Though the major structure isolated experimentally contained an intact Fe_2N_2 core, a second open structure was also identified similar to **Co-1a** (**Fe-1a**).[63] DFT calculations revealed an electronic energy difference of *ca.* 3 kcal mol^{-1} between **Fe-1** and **Fe-1a**, thereby accounting for the ability to isolate both structures.

The formal shortness ratio (FSR), a quantitative assessment of M–M interactions based on single-crystal XRD data,[2] was calculated for each of the complexes by dividing the experimentally determined M–M distance by the sum of the two metal atomic radii.[90] The FSRs for **Co-1** and **Co-2** were determined to be 1.25 and 1.06, respectively, which is opposite of what was observed previously for **Fe-1** (1.08) and **Fe-2** (1.19). In contrast to both Fe and Co, **Mn-1** and **Mn-2** show smaller substituent-dependent differences in M–M distances, as reflected by similar FSR values of 1.15 and 1.20. These values suggest little evidence of metal–metal bonding. In contrast, the shorter FSR value of 1.06 for **Co-2** suggests the possibility of a metal–metal bond, which is corroborated by the electronic structure analysis described in the following sections.

A final observation from the structural studies concerns the stability of **Co-2**. Crystals of a second species isolated from some of the reaction mixtures revealed decomposition of **L2** and formation of a dinuclear species supported by bridging thiolate ligands (**Co-3**; Fig. 5). The structure of **Co-3** revealed oxidation of both Co^{2+} metal ions to Co^{3+} with S–C cleavage and the loss of a methyl group from each ligand. Interestingly, this type of C–S reactivity was observed previously by us in attempts to prepare other Group 9 complexes with Rh and Ir and H_2(**L2**).[91] The coordination geometry around each metal in **Co-3** is distorted square pyramidal (τ_5 = 0.11/0.30) with planar N_2S_2 ligands occupying the equatorial sites and a bridging thiolate occupying the axial site. The Co–Co distance elongates from 2.4540(8) Å in **Co-2** to 3.2172(4) Å in **Co-3**. The Co–S distances associated with the bridging thiolates in the Co_2S_2 core range from 2.2100(6) to 2.2858(5) Å, which are consistent with those reported for Co^{3+} complexes with Co_2S_2 diamond cores bridged by thiolate-containing N_2S_2 and N_2S_3 ligands.[92–95] The bridging Co–thiolate distances in **Co-3** are notably similar to the Co–SMe distances at 2.1906(5) and 2.2234(5) Å. The Co–N distances range from 1.851(2) to 1.900 (2) Å.

Spectroscopic measurements

UV-vis spectra were recorded for all four complexes to assess differences that arise due to changes in the ligands, metal identity, and structures (Fig. 6). The UV region for each of the complexes shows intense, broad features assigned to charge transfer transitions. **Mn-1** and **Co-1** have a more defined transition around 337 nm, matching well with the UV-vis data reported for the dinuclear Fe complexes.[63] **Co-2** exhibits an additional transition at 516 nm that is not observed for the other complexes. A similar feature was observed in the UV-vis spectrum of **Cr-2** at 455 nm. As in our prior study with Cr, this feature may be assigned to metal–metal charge transfer (MMCT). Similar absorptions were reported by Lu and co-workers for a series of metal–metal bonded Co complexes, and this included a dicobalt complex with an absorption at 450 nm that was assigned as either MMCT or metal-to-ligand charge transfer (MLCT).[3,96]

Nuclear magnetic resonance (NMR) spectra of **Mn-1** and **Mn-2** revealed these complexes to be paramagnetic; consistent with high-spin configurations, no ^{1}H resonances were observed even when the window was extended to δ_H ± 200 ppm. The ^{1}H NMR spectrum of **Co-1** also revealed this complex to be paramagnetic, and several paramagnetically shifted resonances were observed in the ^{1}H NMR spectrum at δ_H 61.72, 25.51, 18.01, and −13.34 ppm in C_6D_6 (Fig. S10 and S11; SI). In contrast, the ^{1}H NMR data collected for **Co-2** revealed resolved signals in the typical δ_H 0–12 ppm window, suggesting that the complex is relatively diamagnetic (Fig. 7). Moreover, these results are consistent with prior observations;

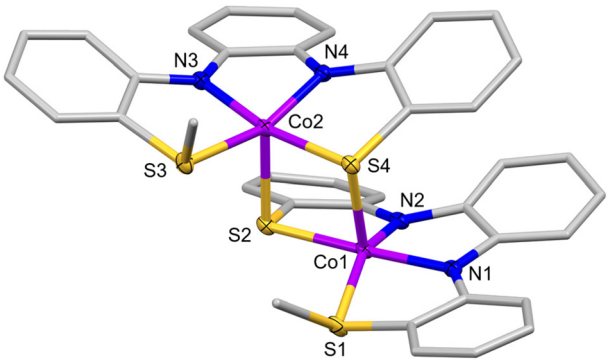

Fig. 5 Molecular structure of **Co-3**. Ellipsoids are drawn at 50% probability. Hydrogen atoms and co-crystallized THF are not shown. Select distances and angles: Co1–Co2 = 3.2172(4) Å, Co1–N1 = 1.900(2) Å, Co1–N2 = 1.851(2) Å, Co2–N3 = 1.883(2) Å, Co2–N4 = 1.860(1) Å, Co1–S1 = 2.1906(5) Å, Co2–S3 = 2.2858(5) Å, Co1–S2 = 2.2100(6) Å, Co2–S2 = 2.2858(5) Å, Co1–S4 = 2.2719(5) Å, Co2–S4 = 2.2161(6) Å, S2–Co1–S4 = 87.49(2)°, S2–Co2–S4 = 87.00(2)°.

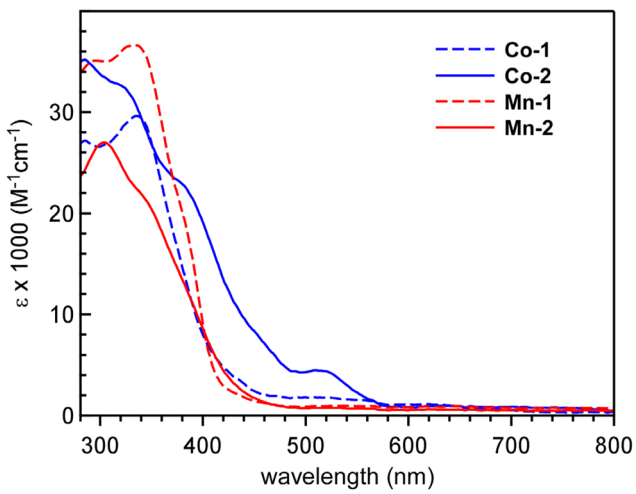

Fig. 6 UV-vis comparison of Mn and Co complexes in C_6H_6.

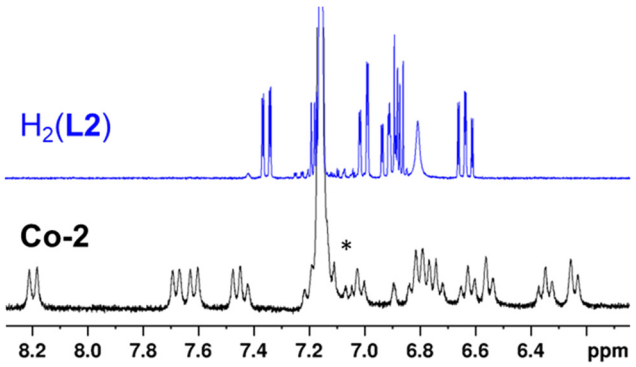

Fig. 7 ^{1}H NMR comparison (aromatic region) of H_2(**L2**) (top; blue) and **Co-2** (bottom; black) in C_6D_6. Asterisk (*) denotes trace toluene impurity in the sample.

Matsuzaka and coworkers reported a dinuclear Co(II) complex containing a similar butterfly-shaped Co_2N_2 core with a Co–Co distance of 2.4276(8) Å,[97] which is slightly shorter than that observed in **Co-2**. This complex also appeared to be diamagnetic by ^{1}H NMR spectroscopy.

Magnetism studies

The magnetic properties of the Mn(II) and Co(II) complexes were assessed using the Evans method[98,99] and compared to previous results obtained for Fe(II) (Table 2). We first compare the Co complexes given the obvious differences in paramagnetism observed during their characterization by ^{1}H NMR spectroscopy. The effective magnetic moment of **Co-1** at room temperature was determined to be $\mu_{eff} = 4.5\mu_B$, consistent with the significant paramagnetism observed in NMR studies. This magnetic moment indicates a spin-only value close to $S = 2$, which suggests approximately two unpaired electrons per Co. Though the ^{1}H NMR spectrum of **Co-2** suggests that it is diamagnetic, the magnetic moment does indicate a small amount of unquenched spin. The Evans method data collected for **Co-2** revealed an effective magnetic moment of $\mu_{eff} = 1.2\mu_B$, which is less than the spin-only magnetic moment for an $S = \frac{1}{2}$ system ($1.73\mu_B$). This relatively low value indicates significant spin pairing between the two d^7 metals. We attribute this to weak Co–Co bonding, which is corroborated by quantum chemical calculations described in the following section (see below).

Table 2 Comparison of formal shortness ratio (FSR), d-electron counts, room-temperature magnetic moments (Evans method), and approximate S values for Mn, Fe, and Co complexes

Complex	FSR	d-Count	μ_{eff} (μ_B)	S
Mn-1	1.15	10	4.6	2
Fe-1 [63]	1.08	12	7.6	3.5
Co-1a	1.25	14	4.5	2
Co-1b	1.14	14	4.5	2
Mn-2	1.20	10	5.6	3
Fe-2 [63]	1.19	12	6.2	3
Co-2	1.06	14	1.2	0.5

Compared to the Co complexes, **Mn-1** and **Mn-2** yielded effective magnetic moments that were more similar at 4.6 and $5.6\mu_B$, respectively. Interestingly, the values show the opposite ordering compared to the Fe complexes with the same ligands. While **Mn-2** had the larger magnetic moment compared to **Mn-1**, **Fe-1** had a higher magnetic moment ($7.6\mu_B$) compared to **Fe-2** ($6.2\mu_B$). It is also clear from Table 2 that the magnetic moments do not correlate with M–M distances or their corresponding formal shortness ratios. This suggests that magnetic moments in dinuclear complexes containing **L1** and **L2** are primarily influenced by superexchange *via* the bridging amido ligands. It is well known that superexchange is governed by structural changes to M–N–M and M–N_{cent}–M angles that alter overlap between 3d-orbitals on the metal and orbitals on the bridging ligand.[100] Orbital overlap is also affected by the bridging M–$N_{bridging}$ distances, which are asymmetric in some complexes and are distinguished by L- and X-type bonding. The competing influences of the M–N–M angles and M–$N_{bridging}$ distances, combined with the differing d-counts and metal-dependent differences in electronic structure, ultimately make it challenging to model the structural influence on the magnetic moments.

As a final assessment of magnetic properties, variable-temperature SQUID data were collected on **Mn-1** and **Mn-2** to quantify the extent of superexchange in these complexes (Fig. 8). Similar data were not collected on **Co-1** and **Co-2** due to concerns about the stability of **Co-2** (and the associated presence of **Co-3**) and because of the differing open and closed structures of **Co-1** that co-crystallize in the solid state.

Variable-temperature magnetic susceptibility ($\chi_M T$) measurements were conducted under an applied dc field of 0.1 T. The behaviors of both **Mn-1** and **Mn-2** are very similar, so we focus here on **Mn-2**, which has data extending down to

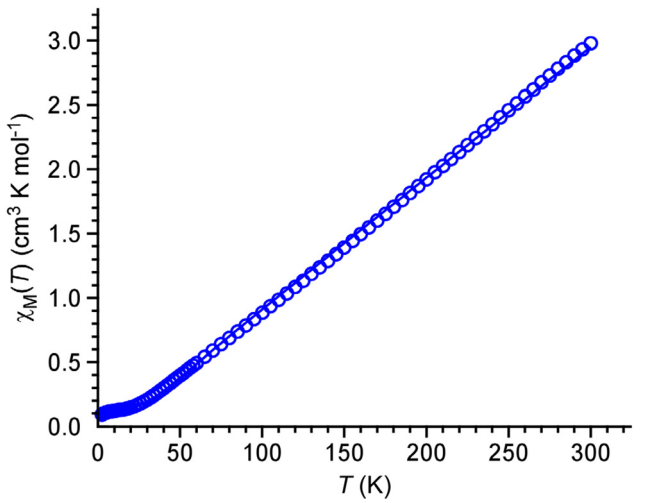

Fig. 8 Solid-state variable-temperature zero-field-cooled (zfc) dc magnetic susceptibility data for **Mn-2** collected under a 0.1 T applied dc field. The solid line represents best fit to the data. **Mn-2**: $S_1 = S_2 = 2.5$, $g_1 = g_2 = 2.1$, $J = -50(0.3)$ cm^{-1}, TIP = 265×10^{-5} cm^3 mol^{-1}: monomeric Mn(II) $S = 2.5$ "impurity" set at 2%.

2.5 K (Fig. 8; data for **Mn-1** are shown in Fig. S4; SI). The room temperature (300 K) $\chi_M T$ value of **Mn-2** is 2.98 cm^3 K mol^{-1}. The $\chi_M T$ value declines linearly with decreasing temperature, resulting in a near zero value at the lowest temperatures probed (0.09 cm^3 K mol^{-1} at 2.5 K for **Mn-2**). Significant intramolecular antiferromagnetic exchange coupling is observed, which was modeled with a J value (using the $-2J$ formalism) of -50 cm^{-1} for **Mn-2**. Similarly, J was found to be -45 cm^{-1} for **Mn-1**. These J values are somewhat higher than, but comparable to, the Fe analogues reported previously at $-0.22(3)$ cm^{-1} (**Fe-1**) and $-37(1)$ cm^{-1} (**Fe-2**).[63] They show substantially weaker coupling than the Cr analogues disclosed recently.[64]

Quantum chemical calculations

Density functional theory (DFT) calculations were performed to explore the bonding within the M_2N_2 cores of **Mn-1**, **Mn-2**, **Co-1a**, **Co-1b**, and **Co-2**. Upon performing full geometry optimizations for **Mn-1**, significant deviations were noted in the bond distances in the Mn_2N_2 core (Tables S5 to S6). First, the percent deviation for the metal–metal distance varied across the functionals tested, from 2.68% with TPSS-D3 to 6.45% with B3LYP-D3. Moreover, within the Mn_2N_2 core, the Mn–N_b distances had a percent deviation ranging from 4.87 ± 7.80% with B3LYP-D3 to 1.46 ± 1.61% with PBE0-D3 (Fig. S21). Similar structural deviations from experiment were obtained for **Mn-2** (Tables S7 to S8), where the metal–metal bond varied across the functionals tested, from 1.75% with TPSS-D3 to 3.82% with BLYP-D3. Though still large, the deviations within the Mn_2N_2 core in the Mn–N_b distances are slightly smaller compared to **Mn-1** ranging from 3.42 ± 4.73% with B3LYP-D3 to 1.62 ± 3.40% with TPSSh-D3 (Fig. S22).

In prior work, small energy differences were noted between **Fe-1** and **Fe-1a**; however, the B3LYP optimized geometries for the more stable of the two, **Fe-1a**, and the complex with the sulfur-based ligand, **Fe-2**, were in sufficiently good agreement with diffraction data.[63] Since the Mn and Fe complexes are expected to behave similarly and functional sensitivity was not tested in the prior work, it was undertaken here for **Fe-1a** and **Fe-2** (Tables S9 to S12). Upon revisiting this system, the average percent deviation from experiment across the eight functionals in **Fe-2** ranges from −14.96% with M06-L to 1.88% with CAM-B3LYP-D3 in the metal–metal distance, though we note that a large underestimation of the bond distance is obtained for PBE-D3 and BLYP-D3 as well at −14.56% and −14.38%, respectively. The deviation in the Fe–N_b bonds is less pronounced, but not negligible, ranging from 0.49 ± 1.00% with M06-L to 1.89 ± 2.61% with B3LYP-D3. Structural deviations were also reported for analogous chromium complexes, where differences were attributed to a very flat potential energy surface along the metal–ligand bond. Since DFT optimized geometries had large deviations from experiment, a constrained geometry optimization was performed using the TPSS-D3 functional in which the positions of the atoms in the Mn_2N_2 core and the first coordination sphere were fixed at the positions from the solid-state diffraction experiments, which are referred to as experimentally-derived structures herein. The constrained and fully optimized DFT structures were within 3.3 kcal mol^{-1} for both Mn and Co complexes with the exception of **Co-2** where a multiconfigurational electronic structure is obtained (Table S16), supporting the conclusion that the differences between DFT arise from small changes in energy that can be influenced by solid state packing. This is also supported by the presence of multiple structures in the solid state (**Fe-1**/**Fe-1a** and **Co-1a**/**Co-1b**). The energy difference between the experimentally derived structures of **Co-1a** and **Co-1b** is only 2.5 kcal mol^{-1}. An alternative explanation is that intramolecular non-covalent interactions between methyl and phenyl C–H bonds with neighboring aryl groups stabilizes particular ligand wrapping modes.[101,102] Indeed, such short contacts are noted in the resulting structures (Fig. S26 to S29). Finally, the DFT spin splitting energies (S = 0 to S = 5 for **Mn-1** and **Mn-2**) are reported (Table S17).

Turning towards the complexes with Co, DFT geometry optimizations were performed with the TPSS-D3 functional for **Co-1a**, **Co-1b**, and **Co-2**. With the exception of the long Co–Co distance, the open **Co-1a** structure gave geometries in reasonable agreement with experiment (Table S13 and Fig. S25); the half-bridged **Co-1b** structure showed −12.75% in the high spin septet state for the metal–metal distance and −4.87 ± 6.40% for the Co–N_b distances (Table S14). Likewise, the "closed" **Co-2** structure in the singlet state had the percent deviations from experiment using TPSS-D3 with −5.75% in the metal–metal distance and 7.01 ± 0.51% for the Co–N_b distances (Table S15). Given that large deviations from experiment were also observed for the Mn and Fe complexes, further functional testing was not expected to result in improved structures for Co; therefore, this was not undertaken herein. Once again, an experimentally derived structure was obtained for all three cobalt complexes. On this structure, DFT spin-splitting energies were computed for the S = 0 to S = 3 states (Table S17). Significant functional dependence was observed, and the ground state could not be assigned from DFT. Moreover, the short Co–Co distance in **Co-2** suggests that a metal–metal interaction could be present, which could lead to multiconfigurational character that would explain the inability of DFT to describe the ground state electronic structure.

To understand the bonding in **Co-2**, restricted active space (RASSCF) calculations were performed. Note that for first row transition metals in which the d-shell is more than half filled, a so-called "double-shell effect" has been reported. To obtain reliable spin-splitting energies with the second-order multireference method (RASPT2), one should include not only the 3d but also the 4d orbitals in the active space. Taking this into account, including 20 orbitals in the active space of a CASSCF calculation for first-row dinuclear transition metal complexes would lead to prohibitively large number of determinants for lower spin states requiring the use of RASSCF (see the Computational details section). The RASPT2 spin splitting energies of **Co-2** (Table 3) result in a ground state singlet with higher spin states increasing in energy step-wise through the septet, which falls at 6.2 kcal mol^{-1}.

Specifically, a direct Co–Co interaction is observed that leads to a highly multiconfigurational singlet ground state dominated by two determinants (the $\sigma^2\sigma^{*0}$ configuration contributing 57.1% and the $\sigma^0\sigma^{*2}$ configuration contributing

Table 3 RASPT2 relative energies in kcal mol^{-1} for **Mn-1**, **Mn-2**, **Co-1a**, **Co-1b**, and **Co-2**. An active space of (10*e*,0*h*,4*e*;0*o*,10*o*,10*o*) is used for the Mn species, using the notation defined by Sauri *et al.*[103] For the Co species, an active space of (14*e*,0*h*,2*e*;0*o*,10*o*,10*o*) is used. All possible spin states accessible within the 3d shell are computed

Spin, S	Mn-1	Mn-2	Co-1a	Co-1b	Co-2
0	0.0	0.0	0.0	0.0	0.0
1	0.4	0.2[a]	0.2	0.4	3.5
2	1.0	0.6	0.5	1.0	5.7
3	1.8	1.1	0.6	1.4	6.2
4	2.8	1.3	—	—	—
5	3.8	2.3	—	—	—

[a] RASSCF orbitals are fixed as those from the single spin state.

34.5% to the total wavefunction). In both configurations, the remaining 12 active electrons are in six doubly occupied 3d orbitals. These types of electron configurations are associated with significant radical character. The active natural orbitals involved in the bond (Fig. 9) have occupation numbers of 1.24 and 0.76, resulting in an effective bond order of 0.24. The effective bond order is related to the percent radical character (% rad) using the following equation:

$$\%\text{rad} = (1 - \text{EBO}) \times 100$$

In **Co-2**, this means the σ-system results in 76% radical character. This can be compared to recent work on **Cr-2** where an effective bond order of 0.73 or 27% radical character was reported.[64] In the Cr complex, three bonding orbitals contribute to this effective single bond; however, it is not only the presence of other orbital interactions that lead to this increase in bond order. The occupation numbers of the σ and σ* orbitals in **Cr-2** are also larger compared to **Co-2** resulting in an EBO of 0.39 or 61% radical character in the σ-system. Returning to **Co-2**, this weak bonding interaction remains present in the triplet state but further weakened to an effective bond order of 0.13 or 87% radical character. On the other hand, no σ-type interactions are obtained in the quintet or septet states.

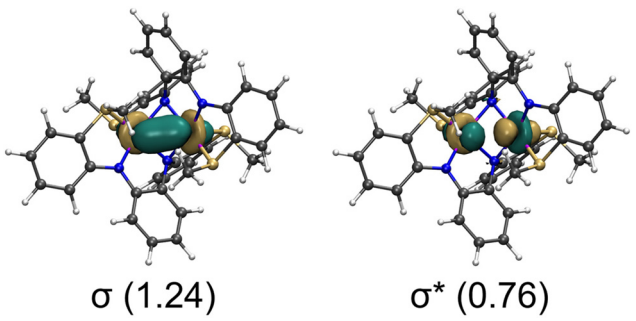

Fig. 9 RASSCF natural orbitals involved in σ-type interactions and their corresponding occupation numbers for the S = 0 state of **Co-2**. 3d orbitals with occupations 1.97 or larger were assigned as doubly occupied. Those with occupation numbers of 0.04 or smaller were assigned as empty. See Fig. S40 for the image of all active orbitals.

Analogous computations were performed for the other complexes: **Mn-1**, **Mn-2**, **Co-1a**, and **Co-1b**. The RASPT2 relative energies (Table 3) support weak coupling between the two metal centers with the lowest energy state being the singlet state and the high spin state being the largest. The difference between the two is only 3.8, 2.3, 0.6, and 1.4 kcal mol^{-1} for **Mn-1**, **Mn-2**, **Co-1a**, and **Co-1b**, respectively. This is consistent with the prior results for the Fe complexes and with the aforementioned magnetic measurements.[63] We note in passing that the use of a limited active space will lead to the overstabilization of the low spin state compared to high spin. Supporting this expectation, tests on these systems of smaller active spaces lead to a larger gap in energy (Table S21), though we note that overstabilization of the low-spin state could remain given the use of an RAS space. Active natural orbitals and occupation numbers are given for all computations in the SI (Fig. S26 to S36). RASSCF wavefunctions are also reported (Tables S22 to S45).

Conclusions

In summary, we have presented the syntheses and characterization studies of dinuclear Mn(II) and Co(II) complexes with triaryl N_4 and N_2S_2 ligands derived from *o*-phenylenediamide. In contrast to previous studies with Fe(II) and Cr(II),[63,64] **Mn-1** and **Mn-2** revealed only relatively modest differences in structures and magnetic properties, but the studies with Co(II) again revealed how relatively modest changes in the ligand flanking groups can give rise to significant differences in molecular structure and the corresponding magnetic properties. Two different dinuclear isomers of **Co-1** with X = NMe_2 were isolated with open (**Co-1a**) and semi-open cores (**Co-1b**), whereas **Co-2** with X = SMe formed a complex with a closed Co_2N_2 diamond core and a relatively short Co–Co distance of 2.4540(8) Å. The changes in structure corresponded to marked differences in magnetic and spectroscopic properties: **Co-2** revealed a low magnetic moment of 1.2μ_B at room temperature, consistent with significant electronic coupling between the metals, whereas the other complexes had significantly higher spin values. Quantum chemical calculations corroborated these experimental observations and suggested a weak Co–Co bond for **Co-2** with an effective bond order of 0.24 or 76% radical character. This is notably similar to the 0.22 effective bond order calculated by Lu, Gagliardi, and coworkers for $Co_2(py_3tren)Cl$,[104] a complex with a Co^{II}–Co^{II} bond distance of 2.4986(4) Å and a diagnostic charge transfer feature like that observed in the UV-vis spectrum of **Co-2**.

Collectively, these studies help to further illuminate the combined influence of metal and ligand donor substituents on the structure of dinuclear complexes with triaryl ligands like **L1** and **L2**. Future efforts are aimed at investigating the reactivity of these and related complexes with first-row transition metals.

Experimental

General considerations

All reactions were performed under nitrogen or argon using a glovebox and standard Schlenk techniques unless stated otherwise. Pentane, Et_2O, and THF were dried and degassed using a Pure Process Technologies solvent purification system and stored over 3 Å molecular sieves. Protio and deuterated benzene were dried over 3 Å molecular sieves and deoxygenated by three freeze–pump–thaw cycles. The ligand precursors H_2(**L1**) (X = NMe_2) and H_2(**L2**) (X = SMe) were synthesized as described previously.[62,105] $Mn_2(Mes)_4(THF)_2$,[70] $Mn_2[N(SiMe_3)_2]_4$,[106] and $Co[N(SiMe_3)_2]_2(THF)$[106] were synthesized following literature methods. All other chemicals were purchased from commercial vendors and used as received.

^{1}H NMR spectra were recorded using a Bruker Avance-300 instrument operating at 300 MHz or a Bruker Avance-500 instrument operating at 500 MHz. Chemical shifts are reported relative to residual solvent peaks in δ_H units.[107] Combustion elemental analysis (CHN) was performed using a CE440 combustion CHN analyzer from Exter Analytical at the University of Iowa MATFab Facility. IR spectra were recorded using a Thermo Scientific Nicolet iS5 instrument with an attenuated total reflectance (ATR) attachment.

Mn-1. To a suspension of $Mn_2(Mes)_4(THF)_2$ (0.290 g, 0.398 mmol) in THF (15 mL) was added H_2(**L1**) (0.275 g, 0.795 mmol). The mixture was stirred overnight during which time the suspension turned dark green. The mixture was evaporated to dryness under vacuum to afford a dark green solid. The solid was extracted with benzene (5 mL) and filtered through a pad of Celite. Vapor diffusion of the benzene filtrate with pentane resulted in green crystals. Yield: 0.157 g (48%). Anal. calcd for $C_{44}H_{48}Mn_2N_8$: C, 66.16; H, 6.06; N, 14.03. Found: C, 64.81; H, 6.08; N, 13.24. Evans method (C_6D_6): 4.6μ_B. IR (ATR, cm^{-1}): 3049, 2909, 1566, 1546, 1477, 1455, 1438, 1428, 1419, 1409, 1363, 1355, 1296, 1246, 1222, 1169, 1152, 1123, 1045, 1027, 962, 950, 914, 869, 859, 829, 752, 742, 735, 683, 595, 587, 568, 558, 549, 529. UV vis (C_6H_6) λ_{max}, nm (ε): 285 nm (ε = 34 500 M^{-1} cm^{-1}).

Mn-2. To a suspension of $MnCl_2$ (0.100 g, 0.795 mmol) in Et_2O (15 mL) was added $Li[N(SiMe_3)_2]$ (0.266 g, 1.59 mmol) dissolved in Et_2O (5 mL). The mixture was stirred overnight and evaporated to dryness under vacuum to yield a tan solid. To the solid was added H_2(**L2**) (0.280 g, 0.795 mmol) dissolved in THF (15 mL). The mixture was stirred overnight during which time the color changed from tan to green. The next day, the volatiles were removed under vacuum to afford a green solid that was extracted with benzene (5 mL) and filtered through a pad of Celite. Vapor diffusion of the green filtrate with pentane yielded green crystals. Yield: 0.216 g (67%). Anal. calcd for $C_{40}H_{36}Mn_2N_4S_4$: C, 59.25; H, 4.48; N, 6.91. Found: C, 58.45; H, 4.39; N, 6.92. Evans method (C_6D_6): 5.6μ_B. IR (ATR, cm^{-1}): 3050, 2909, 1567, 1546, 1477, 1456, 1438, 1428, 1418, 1409, 1364, 1355, 1297, 1246, 1223, 1169, 1152, 1123, 1045, 1027, 962, 950, 914, 869, 859, 829, 752, 742, 735, 683, 595, 587, 568, 558, 549, 529. UV vis (C_6H_6) λ_{max}, nm (ε): 290 nm (ε = 25 000 M^{-1} cm^{-1}).

Co-1. $Co[N(SiMe_3)_2]_2(THF)$ (0.198 g, 0.439 mmol) was added to a Schlenk tube and dissolved in THF (15 mL) with stirring. To the green solution was added H_2(**L1**) (0.152 g, 0.439 mmol) in THF (5 mL). The color immediately changed to dark brown. After stirring overnight, the mixture was evaporated to dryness under vacuum. The dark red brown solid formed was extracted with benzene and filtered through Celite, and the filtrate was evaporated to dryness under vacuum. The material was crystallized in concentrated THF at −30 °C. Yield: 0.131 g (77%). Anal. calcd for $Co_2C_{44}H_{48}N_8\cdot(C_6H_6)_{0.7}$: C, 67.20; H, 6.11; N, 13.01. Found: C, 67.98; H, 6.21; N, 13.46. ^{1}H NMR (300 MHz, C_6D_6): δ_H −13.34 (s), 18.01 (s), 25.51 (s), 61.72 (s). Evans method (C_6D_6): 4.5μ_B. IR (ATR, cm^{-1}): 3087, 3062, 3031, 2913, 2863, 2828, 2795, 2783, 2358, 2340, 1588, 1564, 1475, 1445, 1434, 1398, 1314, 1281, 1259, 1241, 1202, 1182, 1155, 1110, 1094, 1047, 1004, 919, 870, 846, 836, 752, 733, 680, 645, 604, 582. UV vis (C_6H_6) λ_{max}, nm (ε): 337 nm (ε = 33 220 M^{-1} cm^{-1}).

Co-2. The preparation was the same as that described for **Co-1** with $Co[N(SiMe_3)_2]_2(THF)$ (0.256 g, 0.567 mmol) and H_2(**L2**) (0.200 g, 0.567 mmol) in THF. Upon mixing, the color immediately changed from green to dark brown. After stirring overnight, the volatiles were removed under vacuum. The dark brown solid was dissolved in benzene, filtered through Celite, and crystallized out of concentrated benzene at RT or concentrated THF at −30 °C. Yield: 0.115 g (49%). Anal. calcd for $Co_2C_{40}H_{36}N_4S_4$: C, 58.62; H, 4.43; N, 6.84. Found: C, 58.66; H, 4.68; N, 6.50. ^{1}H NMR (500 MHz, C_6D_6): δ_H 0.91 (s), 1.47 (s), 6.29 (m), 6.72 (m), 7.61 (m), 8.19 (s). Evans method (C_6D_6): 1.2μ_B. IR (cm^{-1}): 3049, 1566, 1546, 1476, 1426, 1353, 1325, 1297, 1263, 1244, 1216, 1189, 1169, 1147, 1123, 1044, 1027, 962, 949, 915, 869, 858, 846, 827, 733, 719, 683, 668, 650, 594, 556. UV vis (C_6H_6) λ_{max}, nm (ε): 325 (31 000 M^{-1} cm^{-1}), 388 (22 000 M^{-1} cm^{-1}), 516 (4600 M^{-1} cm^{-1}).

Dark green crystals of **Co-3** sometimes co-crystallize with dark brown **Co-2** when repeating the reaction described above using nearly identical quantities and conditions. We suspect that **Co-3** is always formed in the reaction in low concentrations, and it appears to be a minor product. It is not clear why crystals of **Co-3** are observed in some of these reactions and not others. A possible explanation is that the relative concentration and subtle differences in the rate of crystallization dictate whether it co-crystallizes from the reaction mixture.

Single-crystal X-ray diffraction studies

Data were collected using a Bruker D8 VENTURE DUO diffractometer equipped with an IμS 3.0 microfocus source operated at 75 W (50 kV, 1.5 mA) to generate Mo Kα radiation (λ = 0.71073 Å) and a PHOTON III detector. Crystals were transferred from the vial and placed on a glass slide in type NVH immersion oil from Cargille. A Zeiss Stemi 305 microscope was used to identify a suitable specimen for X-ray diffraction from a representative sample of the material. The crystal and a small amount of the oil were obtained using an MiTeGen 100 micron MicroLoop and transferred to the instrument where it was placed under a cold nitrogen stream (Oxford 800 series) maintained at 100 K throughout the duration of the

experiment. The sample was optically centered with the aid of a video camera to ensure that no translations were observed as the crystal was rotated through all positions.

A unit cell collection was then carried out. After it was determined that the unit cell was not present in the CCDC database, a data collection strategy was calculated using APEX6. The crystal was measured for size, morphology, and color. After data collection, the unit cell was re-determined using a subset of the full data collection. Intensity data were corrected for Lorentz, polarization, and background effects using APEX6. A semi-empirical correction for absorption was applied using SADABS.[108] The program SHELXT was used for the initial structure solution and SHELXL was used for the refinement of the structure.[109,110] Both of these programs were utilized within the OLEX2 software package.[111] Hydrogen atoms bound to carbon atoms were located in the difference Fourier map and were geometrically constrained using the appropriate AFIX commands.

The structure of **Mn-2** was twinned. A twin law was applied with BASF = 0.4. One of the **L2** ligands was partially disordered over two positions.[112] Solvent masks were used for 0.5 and 2.5 co-crystallized benzene molecules for **Co-1** and **Co-2**, respectively, using the SQUEEZE tool in OLEX2.[113]

UV-vis absorption spectroscopy

UV-vis absorption spectra were recorded from 280 nm to 800 nm using an Avantes AvaSpec-ULS2048L StarLine Versatile fiber-optic spectrometer with an AvaLight-DHc light source equipped with deuterium and halogen lamps. The samples were prepared and analyzed under an N_2 atmosphere in a glovebox. Stock solutions were prepared by dissolving *ca.* 2–5 mg of sample in benzene. Stock solutions were then diluted with either 5- or 10 mL volumetric flasks and then transferred to a 1 cm path length quartz cuvette for data collection.

Magnetism studies

Magnetic data for **Mn-1** and **Mn-2** were collected using a Quantum Design MPMS3 magnetometer. Polycrystalline samples were used as received, without further grinding or processing. Samples were prepared in a dinitrogen-filled MBraun glovebox, where polycrystalline materials were sealed in polyethylene bags and mounted in plastic straws. To verify sample purity, variable-field magnetization measurements were performed at 100 K (0–20 kOe); the resulting linear fits of the *M vs. H* data confirmed the absence of ferromagnetic impurities (Fig. S2 and S3; SI). Magnetic susceptibility data for both compounds were collected between 2.5 K (**Mn-1**) or 10 K (**Mn-2**) and 300 K. Data were corrected for the magnetization of the sample holder (plastic bags) by subtracting the susceptibility of an empty plastic bag, and for the diamagnetic contributions of the sample by using Pascal's constants.

Fits of magnetic susceptibility data to spin Hamiltonian models were conducted using the PHI software package.[114] In both cases, we found negative correlations between the exchange coupling (J) and temperature-independent paramagnetism (TIP) parameters. We gave less weight to stronger antiferromagnetic coupling parameters (more negative J values) as TIP values became less realistic. We also noticed that fits giving g values larger than 2.1 resulted in residual values that were lower than the values quoted below, nominally indicating higher quality fits. However, the temperatures for the maxima of χ_M^{-1} *vs.* T plots matched best for the fits that gave g = 2.1. These appear to be examples where the eye determines fit agreement better than the algorithm. In addition, for other Mn(II) complexes with dinuclear species, g ranges from 2.0 to 2.05.[32,115,116]

For **Mn-1**, the best fit obtained from PHI for a symmetric dinuclear species ($S_1 = S_2 = 2.5$) gave $g_1 = g_2 = 2.1$, antiferromagnetic exchange coupling $J = -45(0.3)$ cm^{-1}, and a temperature-independent paramagnetism (TIP) of 292 × 10^{-6} cm^3 mol^{-1}. The residual value of the fit was 0.08042.

For **Mn-2**, the best fit obtained from PHI for a symmetric dinuclear species ($S_1 = S_2 = 2.5$) gave $g_1 = g_2 = 2.1$, antiferromagnetic exchange coupling $J = -50(0.3)$ cm^{-1}, and a temperature-independent paramagnetism (TIP) of 265 × 10^{-5} cm^3 mol^{-1}. The residual value of the fit was 0.03474.

Computational details

DFT calculations were performed using a range of functionals including PBE,[117] PBE0,[118] TPSS,[119] TPSSh,[120] M06-L,[121] B3LYP,[122] and CAM-B3LYP,[123] each evaluated with D3 dispersion corrections.[124] The def2-TZVP basis set was employed for all atoms.[125] The resolution-of-identity (RI) approximation was employed for the Coulomb integrals and an SCF convergence criterion of 1.0 × 10^{-7} a.u. was used.[126] Geometry optimizations and harmonic vibrational frequency calculations were carried out for the high spin states (S = 4 for **Fe-1** and **Fe-2**, S = 5 for **Mn-1** and **Mn-2**, and S = 3 for **Co-1a**), since the presence of a metal–metal bond was less likely and later supported by CASSCF. However, the assignment of ground state spin was more challenging for **Co-1b** and **Co-2**; therefore, geometry optimizations were performed in the S = 0 to 3 states for these complexes using only the TPSS-D3 and TPSSh-D3 functionals. The Cartesian gradient was converged to 1.0 × 10^{-4}. Given the structural flexibility in the M_2N_2 core, the full geometry optimizations were in poor agreement with solid-state measurements; therefore, a second set of geometry optimizations were performed with the TPSSh-D3 functional in which the metal centers and the atoms in the first coordination sphere were kept fixed at the positions determined from diffraction. This approach was recently used successfully in work on a related complex with a Cr_2N_2 core.[64] These structures are referred to as "experimentally-derived" structures and are used for all subsequent analysis. All DFT calculations were performed using the Turbomole 7.8.1 program package.[127,128]

To assess the interaction between the two metal centers, or lack thereof, restricted active space (RASSCF) calculations were performed on the aforementioned experimentally derived structure.[129] The active space included the 3d and 4d orbitals on each of the metal centers, along with their corresponding electrons. The ten 3d orbitals were placed in RAS2 while the ten 4d orbitals were placed in RAS3. No orbitals were placed in

the RAS1 space. Within RAS2, all excitations were included and two excitations were allowed into RAS3. This can be expressed using the notation proposed by Sauri *et al.* as an (n*e*,0*h*,2*e*;0*o*,10*o*,10*o*) active space where n = 10 for complexes with Mn and 14 for those with Co.[103] The all-electron ANO-RCC basis sets of triple-ζ quality were used on the metal centers and atoms in the first coordination sphere but a smaller contraction was used in peripheral atoms.[130,131] Specifically, the following contractions were used: 6s5p3d2f1g for Mn and Co, 5s4p2d1f for S, 4s3p2d1f for N, 2s1p for C, and 1s for H. In addition to the basis set choice, scalar relativistic effects were included *via* the second-order Douglas–Kroll–Hess Hamiltonian. The RASSCF energy was converged to a threshold of 1.0×10^{-7} a.u.

To assign a ground state, second-order perturbation theory was applied to the RASSCF reference wavefunction (RASPT2).[103] The S = 0 to S = 5 spin states were computed for **Mn-1** and **Mn-2**, while the S = 0 to S = 3 states were computed for **Co-1a**, **Co-1b**, and **Co-2**. Note that while the **Fe-1** and **Fe-2** complexes were revisited with respect to the DFT molecular geometries, their electronic structure has already been reported with multireference methods.[63] The zeroth order Hamiltonian was computed using an imaginary shift of 0.2 a.u., and a default value of the IPEA shift of 0.25 was employed.[132] The RASPT2 energy was converged to a threshold of 1.0×10^{-7} a.u. RASSCF and RASPT2 calculations were performed as implemented in the OpenMolcas software package V24.10.[133]

Author contributions

DHD, DS, AKY, and SS: writing – original draft, investigation, and formal analysis. MMW, AG, DKU, MPS, and SKS: investigation and writing – reviewing and editing. SRD and BV: supervision, funding acquisition, formal analysis, and writing – reviewing and editing.

Conflicts of interest

There are no conflicts to declare.

Data availability

A data set collection of computational results including XYZ files of optimized geometries, and input and output files is available at the FigShare repository: http://doi.org/10.6084/m9.figshare.32178018. Supplementary information (SI): tabulated crystallographic data and structure of $Mn[H(\mathbf{L1})]_2$; SQUID magnetometry data; experimental NMR and IR spectra; tabulated data and plots from DFT, CASSCF, and RASSCF calculations; and XYZ files of optimized geometries. See DOI: https://doi.org/10.1039/d6dt00813e.

CCDC 2543836–2543841 contain the supplementary crystallographic data for this paper.[134a–f]

Acknowledgements

DHD, DS, and SRD thank the NSF (CHE-2247235) and ACS-PRF (68706-ND3) for ancillary support of this work. XRD data were collected using the instrument supported by NSF CHE-1828117. SS and MPS thank the NSF (CHE-1956399) and Colorado State University for support of magnetic measurements carried out at the CSU Analytical Research Core facility (RRID: SCR_021758); we acknowledge Dr Indrani Bhowmick (CSU ARC) for valuable discussions regarding PHI fitting. BV thanks the University of Iowa for start up funds supporting computational resources.

References

1 R. H. Duncan Lyngdoh, H. F. Schaefer III and R. B. King, Metal–Metal (MM) Bond Distances and Bond Orders in Binuclear Metal Complexes of the First Row Transition Metals Titanium Through Zinc, *Chem. Rev.*, 2018, **118**, 11626–11706.
2 J. A. Chipman and J. F. Berry, Paramagnetic Metal-Metal Bonded Heterometallic Complexes, *Chem. Rev.*, 2020, **120**, 2409–2447.
3 R. J. Eisenhart, L. J. Clouston and C. C. Lu, Configuring Bonds between First-Row Transition Metals, *Acc. Chem. Res.*, 2015, **48**, 2885–2894.
4 D. C. Powers, M. A. L. Geibel, J. E. M. N. Klein and T. Ritter, Bimetallic Palladium Catalysis: Direct Observation of Pd(III)–Pd(III) Intermediates, *J. Am. Chem. Soc.*, 2009, **131**, 17050–17051.
5 M. S. Ziegler, K. V. Lakshmi and T. D. Tilley, Dicopper Cu(I)Cu(I) and Cu(I)Cu(II) Complexes in Copper-Catalyzed Azide–Alkyne Cycloaddition, *J. Am. Chem. Soc.*, 2017, **139**, 5378–5386.
6 Y.-Y. Zhou and C. Uyeda, Catalytic reductive [4 + 1]-cycloadditions of vinylidenes and dienes, *Science*, 2019, **363**, 857–862.
7 B. Battistella and K. Ray, O_2 and H_2O_2 activations at dinuclear Mn and Fe active sites, *Coord. Chem. Rev.*, 2020, **408**, 213176.
8 P. Haack and C. Limberg, Molecular CuII-O-CuII Complexes: Still Waters Run Deep, *Angew. Chem., Int. Ed.*, 2014, **53**, 4282–4293.
9 J. W. Whittaker, Non-heme manganese catalase - The other' catalase, *Arch. Biochem. Biophys.*, 2012, **525**, 111–120.
10 G. Schenk, N. Mitic, L. R. Gahan, D. L. Ollis, R. P. McGeary and L. W. Guddat, Binuclear Metallohydrolases: Complex Mechanistic Strategies for a Simple Chemical Reaction, *Acc. Chem. Res.*, 2012, **45**, 1593–1603.
11 P. A. Lindahl, Metal–metal bonds in biology, *J. Inorg. Biochem.*, 2012, **106**, 172–178.
12 A. L. Gavrilova and B. Bosnich, Principles of Mononucleating and Binucleating Ligand Design, *Chem. Rev.*, 2004, **104**, 349–384.

13 C. Uyeda and C. M. Farley, Dinickel Active Sites Supported by Redox-Active Ligands, *Acc. Chem. Res.*, 2021, **54**, 3710–3719.
14 M. Sarkar, Binuclear transition metal complexes containing Metal-Metal bonds: Understanding the fundamental aspects and Metal-Metal cooperativity in catalysis, *Inorg. Chim. Acta*, 2024, **572**, 122275.
15 Q. Wang, S. H. Brooks, T. Liu and N. C. Tomson, Tuning metal-metal interactions for cooperative small molecule activation, *Chem. Commun.*, 2021, **57**, 2839–2853.
16 A. B. Kremer and P. Mehrkhodavandi, Dinuclear catalysts for the ring opening polymerization of lactide, *Coord. Chem. Rev.*, 2019, **380**, 35–57.
17 I. G. Powers and C. Uyeda, Metal-Metal Bonds in Catalysis, *ACS Catal.*, 2017, **7**, 936–958.
18 C. M. Thomas, Metal-metal multiple bonds in early/late heterobimetallic complexes: Applications toward small molecule activation and catalysis, *Comments Inorg. Chem.*, 2011, **32**, 14–38.
19 L. Que Jr. and W. B. Tolman, Bis(μ-oxo)dimetal "diamond" cores in copper and iron complexes relevant to biocatalysis, *Angew. Chem., Int. Ed.*, 2002, **41**, 1114–1137.
20 J. Campos, Bimetallic cooperation across the periodic table, *Nat. Rev. Chem.*, 2020, **4**, 696–702.
21 R. M. Haak, S. J. Wezenberg and A. W. Kleij, Cooperative multimetallic catalysis using metallosalens, *Chem. Commun.*, 2010, **46**, 2713–2723.
22 N. P. Mankad, Selectivity Effects in Bimetallic Catalysis, *Chem. – Eur. J.*, 2016, **22**, 5822–5829.
23 M. Navarro, J. J. Moreno, M. Pérez-Jiménez and J. Campos, Small molecule activation with bimetallic systems: a landscape of cooperative reactivity, *Chem. Commun.*, 2022, **58**, 11220–11235.
24 B. G. Cooper, J. W. Napoline and C. M. Thomas, Catalytic Applications of Early/Late Heterobimetallic Complexes, *Catal. Rev.*, 2012, **54**, 1–40.
25 A. R. Fout, Q. Zhao, D. J. Xiao and T. A. Betley, Oxidative Atom-Transfer to a Trimanganese Complex To Form $Mn_6(\mu^6\text{-E})$ (E = O, N) Clusters Featuring Interstitial Oxide and Nitride Functionalities, *J. Am. Chem. Soc.*, 2011, **133**, 16750–16753.
26 T. D. Harris and T. A. Betley, Multi-Site Reactivity: Reduction of Six Equivalents of Nitrite To Give an $Fe_6(NO)_6$ Cluster with a Dramatically Expanded Octahedral Core, *J. Am. Chem. Soc.*, 2011, **133**, 13852–13855.
27 T. M. Powers, A. R. Fout, S.-L. Zheng and T. A. Betley, Oxidative Group Transfer to a Triiron Complex to Form a Nucleophilic μ^3-Nitride, $[Fe_3(\mu^3\text{-N})]$, *J. Am. Chem. Soc.*, 2011, **133**, 3336–3338.
28 Q. Zhao and T. A. Betley, Synthesis and Redox Properties of Triiron Complexes Featuring Strong Fe-Fe Interactions, *Angew. Chem., Int. Ed.*, 2011, **50**, 709–712.
29 Q. Zhao, T. D. Harris and T. A. Betley, $[(HL)_2Fe_6(NCMe)_m]^{n+}$ (m = 0, 2, 4, 6; n = -1, 0, 1, 2, 3, 4, 6): An Electron-Transfer Series Featuring Octahedral Fe_6 Clusters Supported by a Hexaamide Ligand Platform, *J. Am. Chem. Soc.*, 2011, **133**, 8293–8306.
30 E. V. Eames and T. A. Betley, Site-Isolated Redox Reactivity in a Trinuclear Iron Complex, *Inorg. Chem.*, 2012, **51**, 10274–10278.
31 E. V. Eames, T. D. Harris and T. A. Betley, Modulation of magnetic behavior via ligand-field effects in the trigonal clusters $(PhL)Fe_3L^*_3$ (L* = THF, py, PMe_2Ph), *Chem. Sci.*, 2012, **3**, 407–415.
32 A. R. Fout, D. J. Xiao, Q. Zhao, T. D. Harris, E. R. King, E. V. Eames, S.-L. Zheng and T. A. Betley, Trigonal Mn_3 and Co_3 Clusters Supported by Weak-Field Ligands: A Structural, Spectroscopic, Magnetic, and Computational Investigation into the Correlation of Molecular and Electronic Structure, *Inorg. Chem.*, 2012, **51**, 10290–10299.
33 T. M. Powers and T. A. Betley, Testing the Polynuclear Hypothesis: Multielectron Reduction of Small Molecules by Triiron Reaction Sites, *J. Am. Chem. Soc.*, 2013, **135**, 12289–12296.
34 T. M. Powers, N. X. Gu, A. R. Fout, A. M. Baldwin, R. Hernández Sánchez, D. M. Alfonso, Y.-S. Chen, S.-L. Zheng and T. A. Betley, Synthesis of Open-Shell, Bimetallic Mn/Fe Trinuclear Clusters, *J. Am. Chem. Soc.*, 2013, **135**, 14448–14458.
35 R. Hernández Sánchez and T. A. Betley, Meta-Atom Behavior in Clusters Revealing Large Spin Ground States, *J. Am. Chem. Soc.*, 2015, **137**, 13949–13956.
36 R. Hernández Sánchez, S.-L. Zheng and T. A. Betley, Ligand Field Strength Mediates Electron Delocalization in Octahedral $[(HL)_2Fe_6(L')_m]^{n+}$ Clusters, *J. Am. Chem. Soc.*, 2015, **137**, 11126–11143.
37 R. H. Sanchez, A. M. Willis, S.-L. Zheng and T. A. Betley, Synthesis of Well-Defined Bicapped Octahedral Iron Clusters $[(^{tren}L)_2Fe_8(PMe_2Ph)_2]^n$ (n=0,-1), *Angew. Chem., Int. Ed.*, 2015, **54**, 12009–12013.
38 R. Hernández Sánchez, A. K. Bartholomew, T. M. Powers, G. Menard and T. A. Betley, Maximizing Electron Exchange in a $[Fe_3]$ Cluster, *J. Am. Chem. Soc.*, 2016, **138**, 2235–2243.
39 R. H. Sanchez and T. A. Betley, Thermally Persistent High-Spin Ground States in Octahedral Iron Clusters, *J. Am. Chem. Soc.*, 2018, **140**, 16792–16806.
40 A. K. Bartholomew, C. E. Juda, J. N. Nessralla, B. Lin, S. G. Wang, Y.-S. Chen and T. A. Betley, Ligand-Based Control of Single-Site vs. Multi-Site Reactivity by a Trichromium Cluster, *Angew. Chem., Int. Ed.*, 2019, **58**, 5687–5691.
41 A. K. Bartholomew, R. A. Musgrave, K. J. Anderton, C. E. Juda, Y. Dong, W. Bu, S.-Y. Wang, Y.-S. Chen and T. A. Betley, Revealing redox isomerism in trichromium imides by anomalous diffraction, *Chem. Sci.*, 2021, **12**, 15739–15749.
42 L. N. Awaitey, I. E. Arvizo, S.-L. Zheng and T. A. Betley, Hydride Transfer Reactivity of an Open-Shell [Fe3H]-Cluster, *J. Am. Chem. Soc.*, 2025, **147**, 37907–37911.
43 N. P. Litak, S.-L. Zheng, D. Cui and T. A. Betley, Synthesis of a Stable Tricobalt Carbide Cluster, *J. Am. Chem. Soc.*, 2025, **147**, 20056–20062.

44 S. K. Sharma, P. S. May, M. B. Jones, S. Lense, K. I. Hardcastle and C. E. MacBeth, Catalytic dioxygen activation by Co(II) complexes employing a coordinatively versatile ligand scaffold, *Chem. Commun.*, 2011, **47**, 1827–1829.

45 R. Cariou, F. Dahcheh, T. W. Graham and D. W. Stephan, Mononuclear and dinuclear palladium and nickel complexes of phosphinimine-based tridentate ligands, *Dalton Trans.*, 2011, **40**, 4918–4925.

46 O. Villanueva, N. M. Weldy, S. B. Blakey and C. E. MacBeth, Cobalt catalyzed sp3 C–H amination utilizing aryl azides, *Chem. Sci.*, 2015, **6**, 6672–6675.

47 D. Wang, S. V. Lindeman and A. T. Fiedler, Bimetallic Complexes Supported by a Redox-Active Ligand with Fused Pincer-Type Coordination Sites, *Inorg. Chem.*, 2015, **54**, 8744–8754.

48 T. Wu, J. Musgrove, M. A. Siegler and I. Garcia-Bosch, Mononuclear and Dinuclear Copper Complexes of Tridentate Redox-active Ligands with Tunable H-bonding Donors: Structure, Spectroscopy and H^+/e^- Reactivity, *Chem. – Asian J.*, 2021, **16**, 1608–1618.

49 M. K. Osei, B. Lucht, H.-L. Xu, A. Valles, V. M. Espinoza Castro, N. La and R. Hernández Sánchez, Cyclen-Based Octaamine Ligand Supporting the Formation of Dinuclear Metal Compounds, *Inorg. Chem.*, 2025, **64**, 6408–6413.

50 S. Zhang, Q. Wang, L. M. Thierer, A. B. Weberg, M. R. Gau, P. J. Carroll and N. C. Tomson, Tuning Metal-Metal Interactions through Reversible Ligand Folding in a Series of Dinuclear Iron Complexes, *Inorg. Chem.*, 2019, **58**, 12234–12244.

51 T. Liu, M. R. Gau and N. C. Tomson, Mimicking the Constrained Geometry of a Nitrogen-Fixation Intermediate, *J. Am. Chem. Soc.*, 2020, **142**, 8142–8146.

52 A. Z. Spentzos, M. R. Gau, P. J. Carroll and N. C. Tomson, Unusual cyanide and methyl binding modes at a dicobalt macrocycle following acetonitrile C-C bond activation, *Chem. Commun.*, 2020, **56**, 9675–9678.

53 Q. Wang, S. Zhang, P. Cui, A. B. Weberg, L. M. Thierer, B. C. Manor, M. R. Gau, P. J. Carroll and N. C. Tomson, Interdependent Metal-Metal Bonding and Ligand Redox-Activity in a Series of Dinuclear Macrocyclic Complexes of Iron, Cobalt, and Nickel, *Inorg. Chem.*, 2020, **59**, 4200–4214.

54 S. Zhang, P. Cui, T. Liu, Q. Wang, T. J. Longo, L. M. Thierer, B. C. Manor, M. R. Gau, P. J. Carroll, G. C. Papaefthymiou and N. C. Tomson, N-H Bond Formation at a Diiron Bridging Nitride, *Angew. Chem., Int. Ed.*, 2020, **59**, 15215–15219.

55 A. Z. Spentzos and N. C. Tomson, Mapping the Reactivity of Dicobalt Bridging Nitrides in Constrained Geometries, *Inorg. Chem.*, 2021, **60**, 6889–6899.

56 T. Liu, R. P. Murphy, P. J. Carroll, M. R. Gau and N. C. Tomson, C-C σ-Bond Oxidative Addition and Hydrofunctionalization by a Macrocycle-Supported Diiron Complex, *J. Am. Chem. Soc.*, 2022, **144**, 14037–14041.

57 L. M. Thierer, S. H. Brooks, A. B. Weberg, P. Cui, S. Zhang, M. R. Gau, B. C. Manor, P. J. Carroll and N. C. Tomson, Macrocycle-Induced Modulation of Internuclear Interactions in Homobimetallic Complexes, *Inorg. Chem.*, 2022, **61**, 6263–6280.

58 S. H. Brooks, C. A. Richards, P. J. Carroll, M. R. Gau and N. C. Tomson, Anion Capture at the Open Core of a Geometrically Flexible Dicopper(II,II) Macrocycle Complex, *Inorganics*, 2023, **11**, 348.

59 A. Z. Spentzos, S. A. Ford, B. Muldowney, T. Liu, P. Cui, M. R. Gau, P. J. Carroll and N. C. Tomson, Reactivity Profile of a Formally Dicobalt(0) Complex Bound by a Redox-Active Macrocycle, *Organometallics*, 2024, **43**, 1425–1437.

60 Q. Wang, R. P. Murphy, M. R. Gau, P. J. Carroll and N. C. Tomson, Controlling the Size of Molecular Copper Clusters Supported by a Multinucleating Macrocycle, *Inorg. Chem.*, 2024, **63**, 18332–18344.

61 S. P. Rumi, J. M. Laddusaw, L. N. Zakharov, P. H.-Y. Cheong and A. N. Desnoyer, Well-Defined *syn* Multimetallic Complexes Supported by a Geometrically Flexible Tetraamidodiamine Ligand, *Inorg. Chem.*, 2025, **64**, 23215–23224.

62 K. D. Spielvogel, E. J. Coughlin, H. Petras, J. A. Luna, A. Benson, C. M. Donahue, A. Kibasa, K. Lee, R. Salacinski, S. C. Bart, S. K. Shaw, J. J. Shepherd and S. R. Daly, The Influence of Redox-Innocent Donor Groups in Tetradentate Ligands Derived from *o*-Phenylenediamine: Electronic Structure Investigations with Nickel, *Inorg. Chem.*, 2019, **58**, 12756–12774.

63 K. D. Spielvogel, E. J. Campbell, S. R. Chowdhury, F. Benner, S. Demir, G. P. Hatzis, H. R. Petras, D. Sembukuttiarachchige, J. J. Shepherd, C. M. Thomas, B. Vlaisavljevich and S. R. Daly, Modulation of Fe–Fe distance and spin in diiron complexes using tetradentate ligands with different flanking donors, *Chem. Commun.*, 2024, **60**, 8399–8402.

64 J. L. A. N. Durage, J. Cardona, S. Sinhababu, D. H. Duffy, D. Martinez, M. P. Shores, D. K. Unruh, B. Vlaisavljevich and S. R. Daly, Leveraging Chelating Amido Ligands to Support Metal-Metal Bonding in Dinuclear Cr(II) Complexes, *Inorg. Chem.*, 2026, **65**, 5850–5863.

65 K. D. Spielvogel, E. J. Campbell, S. R. Chowdhury, F. Benner, S. Demir, G. P. Hatzis, H. R. Petras, D. Sembukuttiarachchige, J. J. Shepherd, C. M. Thomas, B. Vlaisavljevich and S. R. Daly, Modulation of Fe–Fe distance and spin in diiron complexes using tetradentate ligands with different flanking donors, *Chem. Commun.*, 2024, **60**, 8399–8402.

66 A. M. Bryan, G. J. Long, F. Grandjean and P. P. Power, Synthesis, Spectroscopic Characterization, and, Determination of the Solution Association Energy of the Dimer $[Co\{N(SiMe_3)_2\}_2]_2$: Magnetic Studies of Low-Coordinate Co(II) Silylamides $[Co\{N(SiMe_3)_2\}_2L]$ (L = PMe_3, Pyridine, and THF) and Related Species That Reveal Evidence of Very Large Zero-Field Splittings, *Inorg. Chem.*, 2013, **52**, 12152–12160.

67 A. Eichhöfer, Y. Lan, V. Mereacre, T. Bodenstein and F. Weigend, Slow Magnetic Relaxation in Trigonal-Planar Mononuclear Fe(II) and Co(II) Bis(trimethylsilyl)amido

Complexes—A Comparative Study, *Inorg. Chem.*, 2014, **53**, 1962–1974.

68 D. C. Bradley, M. B. Hursthouse, K. M. A. Malik and R. Möseler, The crystal molecular structure of "bis(hexamethyldisilylamido) manganese", *Transition Met. Chem.*, 1978, **3**, 253–254.

69 B. D. Murray and P. P. Power, Three-coordinate metal amides of manganese(II) and cobalt(II): synthesis and x-ray structure of the first tris(silylamide) of manganese and the x-ray crystal structures of $[M_2(N(SiMe_3)_2)_4]$ (M = Mn, Co), *Inorg. Chem.*, 1984, **23**, 4584–4588.

70 R. Fischer, H. Görls, M. Friedrich and M. Westerhausen, Reinvestigation of arylmanganese chemistry – Synthesis and molecular structures of $[(THF)_4Mg(\mu\text{-}Cl)_2Mn(Br)Mes]$, $[Mes(THF)Mn(\mu\text{-}Mes)]_2$, and $(MnPh_2)_\infty$ (Ph=C_6H_5; Mes = mesityl, 2,4,6-$Me_3C_6H_2$), *J. Organomet. Chem.*, 2009, **694**, 1107–1111.

71 A. W. Addison, T. N. Rao, J. Reedijk, J. van Rijn and G. C. Verschoor, Synthesis, structure, and spectroscopic properties of copper(II) compounds containing nitrogen–sulphur donor ligands; the crystal and molecular structure of aqua[1,7-bis(N-methylbenzimidazol-2′-yl)-2,6-dithiaheptane]copper(II) perchlorate, *J. Chem. Soc., Dalton Trans.*, 1984, 1349–1356.

72 A. G. Blackman, E. B. Schenk, R. E. Jelley, E. H. Krenske and L. R. Gahan, Five-coordinate transition metal complexes and the value of τ_5: observations and caveats, *Dalton Trans.*, 2020, **49**, 14798–14806.

73 M. R. Elsby, M. Son, C. Oh, J. Martin, M.-H. Baik and R. T. Baker, Mechanistic Study of Metal–Ligand Cooperativity in Mn(II)-Catalyzed Hydroborations: Hemilabile SNS Ligand Enables Metal Hydride-Free Reaction Pathway, *ACS Catal.*, 2021, **11**, 9043–9051.

74 Y. Hameed, S. Ouanounou, T. Jurca, B. Gabidullin, I. Korobkov and D. Richeson, Dimers, monomers and pentacoordination in a series of earth-abundant transition metal dibromido complexes supported by a neutral SNS ligand framework, *Polyhedron*, 2018, **154**, 252–258.

75 P. Wang, G. P. A. Yap and C. G. Riordan, Five-coordinate MII-semiquinonate (M = Fe, Mn, Co) complexes: reactivity models of the catechol dioxygenases, *Chem. Commun.*, 2014, **50**, 5871–5873.

76 C. Reus, K. Ruth, S. Tüllmann, M. Bolte, H.-W. Lerner, B. Weber, M. C. Holthausen and M. Wagner, Synthesis, Molecular Structure, and, Physical Properties of the Complexes $[\{PhB(pz)_2(CH_2SMe)\}_2M]$ (M = MnII, FeII; pz = pyrazol-1-yl) Containing a Novel [N,N,S]-Heteroscorpionate Ligand, *Eur. J. Inorg. Chem.*, 2011, 1709–1718.

77 L. R. Gahan, V. A. Grillo, T. W. Hambley, G. R. Hanson, C. J. Hawkins, E. M. Proudfoot, B. Moubaraki, K. S. Murray and D. Wang, Synthetic, X-ray Structure, Electron Paramagnetic Resonance, and Magnetic Studies of the Manganese(II) Complex of 1-Thia-4,7-diazacyclononane ([9]aneN_2S), *Inorg. Chem.*, 1996, **35**, 1039–1044.

78 S. Karmakar, S. B. Choudhury and A. Chakravorty, Thioether Binding of Low-Spin Bivalent Manganese. A MS_2N_4 Family Furnished by New Hexadentate Thioether-Oxime-Azo Ligands (M = MnII, FeII, FeIII), *Inorg. Chem.*, 1994, **33**, 6148–6153.

79 P. Chakraborty, S. K. Chandra and A. Chakravorty, Thioether binding of manganese oxidation states. Chemistry of an $MnII,IIIS_2N_2O_2$ family, *Inorg. Chem.*, 1993, **32**, 5349–5353.

80 E. V. Eames, R. Hernández Sánchez and T. A. Betley, Metal Atom Lability in Polynuclear Complexes, *Inorg. Chem.*, 2013, **52**, 5006–5012.

81 H. Hope, M. M. Olmstead, B. D. Murray and P. P. Power, Syntheses and x-ray structures of the lithium, nickel, and cobalt complexes $[Li(THF)_4][Ni(NPh_2)_3].0.5C_7H_8$, $[\{Ni(NPh_2)_2\}_2]$ and $[\{Co(NPh_2)_2\}_2]$: structural characterization of three coordinate first row d^7 and d^8 complexes, *J. Am. Chem. Soc.*, 1985, **107**, 712–713.

82 D. B. Leznoff, G. Mund, K. C. Jantunen, P. H. Bhatia, A. J. Gabert and R. J. Batchelor, Dinuclear Iron, Cobalt and Uranium Complexes of New Diamidoether Ligands, *J. Nucl. Sci. Technol.*, 2002, **39**, 406–409.

83 G. Zhang, J. Wu, M. Wang, H. Zeng, J. Cheng, M. C. Neary and S. Zheng, Cobalt-Catalyzed Regioselective Hydroboration of Terminal Alkenes, *Eur. J. Inorg. Chem.*, 2017, 5814–5818.

84 D. Zanders, N. Boysen, M. A. Land, J. Obenlüneschloß, J. D. Masuda, B. Mallick, S. T. Barry and A. Devi, Co(II) Amide, Pyrrolate, and Aminopyridinate Complexes: Assessment of their Manifold Structural Chemistry and Thermal Properties, *Eur. J. Inorg. Chem.*, 2021, 5119–5136.

85 N. Jin, A. Logallo and E. Hevia, Structural and Reactivity Implications of Homo- and Heterobimetallic Co(II) Amides Prepared via Trans(amination), Reactions, *Organometallics*, 2025, **44**, 197–206.

86 A. Logallo, L. C. H. Maddock, M. Mu, L. Gravogl, N. Jin, M. N. Peñas-Defrutos, K. Meyer, M. García-Melchor and E. Hevia, Unlocking the Metalation Applications of TMP-powered Fe and Co(II) bis(amides): Synthesis, Structure and Mechanistic Insights, *Angew. Chem., Int. Ed.*, 2024, e202402907.

87 C. R. Stennett and P. P. Power, Hydrides, Halides, and Polymers: Some Unexpected Intermediates on the Routes to First-Row Transition Metal $M\{N(SiMe_3)_2\}_n$ (n = 2, 3) Complexes, *Inorg. Chem.*, 2021, **60**, 18503–18511.

88 L. Yang, D. R. Powell and R. P. Houser, Structural variation in copper(I) complexes with pyridylmethylamide ligands: structural analysis with a new four-coordinate geometry index, τ_4, *Dalton Trans.*, 2007, 955–964.

89 A. Okuniewski, D. Rosiak, J. Chojnacki and B. Becker, Coordination polymers and molecular structures among complexes of mercury(II) halides with selected 1-benzoylthioureas, *Polyhedron*, 2015, **90**, 47–57.

90 L. Pauling, Atomic Radii and Interatomic Distances in Metals, *J. Am. Chem. Soc.*, 1947, **69**, 542–553.

91 K. D. Spielvogel, G. Durgaprasad and S. R. Daly, Configurational Flexibility of a Triaryl-Supported SBS Ligand with Rh and Ir: Structural Investigations and Olefin Isomerization Catalysis, *Organometallics*, 2022, **41**, 1344–1352.

92 J. C. Noveron, M. M. Olmstead and P. K. Mascharak, Co(III) Complexes with Carboxamido N and Thiolato S Donor Centers: Models for the Active Site of Co-Containing Nitrile Hydratases, *J. Am. Chem. Soc.*, 1999, **121**, 3553–3554.
93 L. A. Tyler, M. M. Olmstead and P. K. Mascharak, Thioether ligation in Co(III) complexes with carboxamido nitrogens as donors: implications on the coordination structure of the cobalt site in nitrile hydratase, *Inorg. Chim. Acta*, 2001, **321**, 135–141.
94 B. W. Smucker, M. J. VanStipdonk and D. M. Eichhorn, Incorporation of thiolate donation using 2,2′-dithiodibenzaldehyde: Complexes of a pentadentate N_2S_3 ligand with relevance to the active site of Co nitrile hydratase, *J. Inorg. Biochem.*, 2007, **101**, 1537–1542.
95 A. Panja, C. Campana, C. Leavitt, M. J. V. Stipdonk and D. M. Eichhorn, Iron and cobalt complexes of 2,6-diacetylpyridine-bis(R-thiosemicarbazone) (R=H, phenyl) showing unprecedented ligand deviation from planarity, *Inorg. Chim. Acta*, 2009, **362**, 1348–1354.
96 S. J. Tereniak, R. K. Carlson, L. J. Clouston, V. G. Young Jr, E. Bill, R. Maurice, Y.-S. Chen, H. J. Kim, L. Gagliardi and C. C. Lu, Role of the Metal in the Bonding and Properties of Bimetallic Complexes Involving Manganese, Iron, and Cobalt, *J. Am. Chem. Soc.*, 2014, **136**, 1842–1855.
97 S. Takemoto, T. Honma and H. Matsuzaka, Dinuclear Cp*Co Amido and Alkoxo Complexes: Synthesis, Structures, and Reactivity, *Organometallics*, 2011, **30**, 1013–1020.
98 D. F. Evans, 400. The determination of the paramagnetic susceptibility of substances in solution by nuclear magnetic resonance, *J. Chem. Soc.*, 1959, 2003–2005.
99 M. Uchida, C. H. Cortney, K. Bustos, E. Manzo, E. Sauls, J. Bouchard, R. Fukazawa and V. V. Krishnan, Discovery-Based Approach to Identify Multiple Factors That Affect the Spin State of Coordination Complexes Using the Evans NMR Method, *J. Chem. Educ.*, 2023, **100**, 4822–4827.
100 P. J. Hay, J. C. Thibeault and R. Hoffmann, Orbital interactions in metal dimer complexes, *J. Am. Chem. Soc.*, 1975, **97**, 4884–4899.
101 D. J. Liptrot and P. P. Power, London dispersion forces in sterically crowded inorganic and organometallic molecules, *Nat. Rev. Chem.*, 2017, **1**, 0004.
102 A. N. Brown, J. N. Kelleher, A. M. Brown, P. Saghy, J. J. Bohl, J. R. Robinson and D. N. Huh, Synthesis and reduction of $[(C_5H_4SiMe_3)_2Ln(\mu\text{-}OR)]_2$ (Ln = La, Ce) complexes: structural effects of bridging alkoxides, *Dalton Trans.*, 2024, **53**, 18856–18864.
103 V. Sauri, L. Serrano-Andrés, A. R. M. Shahi, L. Gagliardi, S. Vancoillie and K. Pierloot, Multiconfigurational Second-Order Perturbation Theory Restricted Active Space (RASPT2) Method for Electronic Excited States: A Benchmark Study, *J. Chem. Theory Comput.*, 2011, **7**, 153–168.
104 S. J. Tereniak, R. K. Carlson, L. J. Clouston, V. G. Young, E. Bill, R. Maurice, Y.-S. Chen, H. J. Kim, L. Gagliardi and C. C. Lu, Role of the Metal in the Bonding and Properties of Bimetallic Complexes Involving Manganese, Iron, and Cobalt, *J. Am. Chem. Soc.*, 2014, **136**, 1842–1855.
105 G. Durgaprasad, J. A. Luna, K. D. Spielvogel, C. Haas, S. K. Shaw and S. R. Daly, Ru(II) Complexes with a Chemical and Redox-Active S_2N_2 Ligand: Structures, Electrochemistry, and Metal–Ligand Cooperativity, *Organometallics*, 2017, **36**, 4020–4031.
106 R. A. Andersen, A. M. Bryan, M. Faust, P. P. Power, A. M. Bryan, P. P. Power, R. A. Andersen, M. Faust, P. P. Power and R. A. Andersen, Divalent Manganese, Iron, and Cobalt Bis(trimethylsilyl)amido Derivatives and Their Tetrahydrofuran Complexes, in *Inorganic Syntheses*, 2018, pp. 1–14.
107 H. E. Gottlieb, V. Kotlyar and A. Nudelman, NMR Chemical Shifts of Common Laboratory Solvents as Trace Impurities, *J. Org. Chem.*, 1997, **62**, 7512–7515.
108 G. Sheldrick, *SADABS v2016/2*, University of Göttingen, Germany, 2016.
109 G. M. Sheldrick, SHELXT - Integrated space-group and crystal-structure determination, *Acta Crystallogr., Sect. A: Found. Adv.*, 2015, **71**, 3–8.
110 G. M. Sheldrick, Crystal structure refinement with SHELXL, *Acta Crystallogr., Sect. C: Struct. Chem.*, 2015, **71**, 3–8.
111 O. V. Dolomanov, L. J. Bourhis, R. J. Gildea, J. A. K. Howard and H. Puschmann, OLEX2: a complete structure solution, refinement and analysis program, *J. Appl. Crystallogr.*, 2009, **42**, 339–341.
112 L. J. Bourhis, O. V. Dolomanov, R. J. Gildea, J. A. K. Howard and H. Puschmann, The anatomy of a comprehensive constrained, restrained refinement program for the modern computing environment - Olex2 dissected, *Acta Crystallogr., Sect. A: Found. Adv.*, 2015, **71**, 59–75.
113 A. L. Spek, PLATON SQUEEZE: a tool for the calculation of the disordered solvent contribution to the calculated structure factors, *Acta Crystallogr., Sect. C: Struct. Chem.*, 2015, **71**, 9–18.
114 N. F. Chilton, R. P. Anderson, L. D. Turner, A. Soncini and K. S. Murray, PHI: A powerful new program for the analysis of anisotropic monomeric and exchange-coupled polynuclear d- and f-block complexes, *J. Comput. Chem.*, 2013, **34**, 1164–1175.
115 D. Huang, W. Wang, X. Zhang, C. Chen, F. Chen, Q. Liu, D. Liao, L. Li and L. Sun, Synthesis, Structural Characterizations and Magnetic Properties of a Series of Mono-, Di- and Polynuclear Manganese Pyridinecarboxylate Compounds, *Eur. J. Inorg. Chem.*, 2004, 1454–1464.
116 R. A. Lewis, S. Morochnik, A. Chapovetsky, G. Wu and T. W. Hayton, Synthesis and Characterization of $[M_2(N{=}C\mathit{t}Bu_2)_5]^-$ (M=Mn, Fe, Co): Metal Ketimide Complexes with Strong Metal–Metal Interactions, *Angew. Chem., Int. Ed.*, 2012, **51**, 12772–12775.
117 J. P. Perdew, K. Burke and M. Ernzerhof, Generalized Gradient Approximation Made Simple, *Phys. Rev. Lett.*, 1996, **77**, 3865–3868.
118 J. P. Perdew, M. Ernzerhof and K. Burke, Rationale for mixing exact exchange with density functional approximations, *J. Chem. Phys.*, 1996, **105**, 9982–9985.

119 J. Tao, J. P. Perdew, V. N. Staroverov and G. E. Scuseria, Climbing the Density Functional Ladder: Nonempirical Meta–Generalized Gradient Approximation Designed for Molecules and Solids, *Phys. Rev. Lett.*, 2003, **91**, 146401.
120 V. N. Staroverov, G. E. Scuseria, J. Tao and J. P. Perdew, Comparative assessment of a new nonempirical density functional: Molecules and hydrogen-bonded complexes, *J. Chem. Phys.*, 2003, **119**, 12129–12137.
121 Y. Zhao and D. G. Truhlar, The M06 suite of density functionals for main group thermochemistry, thermochemical kinetics, noncovalent interactions, excited states, and transition elements: two new functionals and systematic testing of four M06-class functionals and 12 other functionals, *Theor. Chem. Acc.*, 2008, **120**, 215–241.
122 A. D. Becke, A new mixing of Hartree–Fock and local density–functional theories, *J. Chem. Phys.*, 1993, **98**, 1372–1377.
123 T. Yanai, D. P. Tew and N. C. Handy, A new hybrid exchange–correlation functional using the Coulomb-attenuating method (CAM-B3LYP), *Chem. Phys. Lett.*, 2004, **393**, 51–57.
124 S. Grimme, J. Antony, S. Ehrlich and H. Krieg, A consistent and accurate ab initio parametrization of density functional dispersion correction (DFT-D) for the 94 elements H-Pu, *J. Chem. Phys.*, 2010, **132**, 154104.
125 F. Weigend and R. Ahlrichs, Balanced basis sets of split valence, triple zeta valence and quadruple zeta valence quality for H to Rn: Design and assessment of accuracy, *Phys. Chem. Chem. Phys.*, 2005, **7**, 3297–3305.
126 A. M. Burow, M. Sierka and F. Mohamed, Resolution of identity approximation for the Coulomb term in molecular and periodic systems, *J. Chem. Phys.*, 2009, **131**, 214101.
127 Y. J. Franzke, C. Holzer, J. H. Andersen, T. Begušić, F. Bruder, S. Coriani, F. Della Sala, E. Fabiano, D. A. Fedotov, S. Fürst, S. Gillhuber, R. Grotjahn, M. Kaupp, M. Kehry, M. Krstić, F. Mack, S. Majumdar, B. D. Nguyen, S. M. Parker, F. Pauly, A. Pausch, E. Perlt, G. S. Phun, A. Rajabi, D. Rappoport, B. Samal, T. Schrader, M. Sharma, E. Tapavicza, R. S. Treß, V. Voora, A. Wodyński, J. M. Yu, B. Zerulla, F. Furche, C. Hättig, M. Sierka, D. P. Tew and F. Weigend, TURBOMOLE: Today and Tomorrow, *J. Chem. Theory Comput.*, 2023, **19**, 6859–6890.
128 TURBOMOLE V6.2 2010, a development of University of Karlsruhe and Forschungszentrum Karlsruhe GmbH, 1989–2007, TURBOMOLE GmbH, since 2007; available from https://www.turbomole.com.
129 P. A. Malmqvist, A. Rendell and B. O. Roos, The restricted active space self-consistent-field method, implemented with a split graph unitary group approach, *J. Phys. Chem.*, 1990, **94**, 5477–5482.
130 B. O. Roos, R. Lindh, P.-Å. Malmqvist, V. Veryazov and P.-O. Widmark, Main Group Atoms and Dimers Studied with a New Relativistic ANO Basis Set, *J. Phys. Chem. A*, 2004, **108**, 2851–2858.
131 B. O. Roos, R. Lindh, P.-Å. Malmqvist, V. Veryazov and P.-O. Widmark, New Relativistic ANO Basis Sets for Transition Metal Atoms, *J. Phys. Chem. A*, 2005, **109**, 6575–6579.
132 G. Ghigo, B. O. Roos and P.-Å. Malmqvist, A modified definition of the zeroth-order Hamiltonian in multiconfigurational perturbation theory (CASPT2), *Chem. Phys. Lett.*, 2004, **396**, 142–149.
133 G. Li Manni, I. F. Galván, A. Alavi, F. Aleotti, F. Aquilante, J. Autschbach, D. Avagliano, A. Baiardi, J. J. Bao, S. Battaglia, L. Birnoschi, A. Blanco-González, S. I. Bokarev, R. Broer, R. Cacciari, P. B. Calio, R. K. Carlson, R. Carvalho Couto, L. Cerdán, L. F. Chibotaru, N. F. Chilton, J. R. Church, I. Conti, S. Coriani, J. Cuéllar-Zuquin, R. E. Daoud, N. Dattani, P. Decleva, C. de Graaf, M. G. Delcey, L. De Vico, W. Dobrautz, S. S. Dong, R. Feng, N. Ferré, M. Filatov, L. Gagliardi, M. Garavelli, L. González, Y. Guan, M. Guo, M. R. Hennefarth, M. R. Hermes, C. E. Hoyer, M. Huix-Rotllant, V. K. Jaiswal, A. Kaiser, D. S. Kaliakin, M. Khamesian, D. S. King, V. Kochetov, M. Krośnicki, A. A. Kumaar, E. D. Larsson, S. Lehtola, M.-B. Lepetit, H. Lischka, P. López Ríos, M. Lundberg, D. Ma, S. Mai, P. Marquetand, I. C. D. Merritt, F. Montorsi, M. Mörchen, A. Nenov, V. H. A. Nguyen, Y. Nishimoto, M. S. Oakley, M. Olivucci, M. Oppel, D. Padula, R. Pandharkar, Q. M. Phung, F. Plasser, G. Raggi, E. Rebolini, M. Reiher, I. Rivalta, D. Roca-Sanjuán, T. Romig, A. A. Safari, A. Sánchez-Mansilla, A. M. Sand, I. Schapiro, T. R. Scott, J. Segarra-Martí, F. Segatta, D.-C. Sergentu, P. Sharma, R. Shepard, Y. Shu, J. K. Staab, T. P. Straatsma, L. K. Sørensen, B. N. C. Tenorio, D. G. Truhlar, L. Ungur, M. Vacher, V. Veryazov, T. A. Voß, O. Weser, D. Wu, X. Yang, D. Yarkony, C. Zhou, J. P. Zobel and R. Lindh, The OpenMolcas Web: A Community-Driven Approach to Advancing Computational Chemistry, *J. Chem. Theory Comput.*, 2023, **19**, 6933–6991.
134 (*a*) CCDC 2543836: Experimental Crystal Structure Determination, 2026, DOI: 10.5517/ccdc.csd.cc2rd27h; (*b*) CCDC 2543837: Experimental Crystal Structure Determination, 2026, DOI: 10.5517/ccdc.csd.cc2rd28j; (*c*) CCDC 2543838: Experimental Crystal Structure Determination, 2026, DOI: 10.5517/ccdc.csd.cc2rd29k; (*d*) CCDC 2543839: Experimental Crystal Structure Determination, 2026, DOI: 10.5517/ccdc.csd.cc2rd2bl; (*e*) CCDC 2543840: Experimental Crystal Structure Determination, 2026, DOI: 10.5517/ccdc.csd.cc2rd2cm; (*f*) CCDC 2543841: Experimental Crystal Structure Determination, 2026, DOI: 10.5517/ccdc.csd.cc2rd2dn.